

AD-A281 745



STATION PAGE

Form Approved  
OMB No. 0704 0188

Do not fill in this box unless you are submitting a report. If you are submitting a report, fill in this box with the following information: Send a letter to the Director, Defense Information Systems Agency, 1215 Jefferson Davis Highway, Arlington, VA 22202, for information on the Defense Information System (DIS) and the Defense Information System (DIS) and the Defense Information System (DIS).

AT DATE

3. REPORT TYPE AND DATES COVERED

THESIS/DISSERTATION

4. TITLE AND SUBTITLE  
Modeling Sea-Surface Variability Caused  
by Kilometer-Scale Marine Atmospheric Boundary  
Layer Circulations.

5. FUNDING NUMBERS

6. AUTHOR(S)

Capt. Louis Vincent Zuccarello

7. PERFORMING ORGANIZATION NAME(S) AND ADDRESS(ES)

AFIT Student Attending:

Pennsylvania State University

8. PERFORMING ORGANIZATION  
REPORT NUMBER

AFIT/CI/CIA-

94-005

9. SPONSORING/MONITORING AGENCY NAME(S) AND ADDRESS(ES)

DEPARTMENT OF THE AIR FORCE

AFIT/CI

2950 P STREET

WRIGHT-PATTERSON AFB OH 45433-7765

10. SPONSORING/MONITORING  
AGENCY REPORT NUMBER

94-22523

11. SUPPLEMENTARY NOTES

12a. DISTRIBUTION/AVAILABILITY STATEMENT

Approved for Public Release IAW 190-1  
Distribution Unlimited  
MICHAEL M. BRICKER, SMSgt, USAF  
Chief Administration

DTIC  
ELECTE  
JUL 20 1994

12b. DISTRIBUTION CODE

13. ABSTRACT (Maximum 200 words)

DTIC QUALITY INSPECTED 5

94 7 19 0 13

14. SUBJECT TERMS

15. NUMBER OF PAGES

16. PRICE CODE

17. SECURITY CLASSIFICATION  
OF REPORT18. SECURITY CLASSIFICATION  
OF THIS PAGE19. SECURITY CLASSIFICATION  
OF ABSTRACT

20. LIMITATION OF ABSTRACT

94-025

Author: Louis Vincent Zuccarello

Title: Modeling Sea-Surface Stress Variability Caused By Kilometer-Scale Marine  
Atmospheric Boundary Layer Circulations

Military Rank: Captain

Service Branch: Air Force

Date: 1994

Number of Pages: 64

Degree Awarded: Master of Science

Name of Institution: The Pennsylvania State University

Accession For	
NTIS	CRA&I <input checked="checked" type="checkbox"/>
DTIC	TAB <input checked="checked" type="checkbox"/>
Unannounced	<input type="checkbox"/>
Justification _____	
By _____	
Distribution /	
Availability Codes	
Dist	Avail and/or Special
A-1	

## ABSTRACT

The interpretation of satellite- or aircraft-borne synthetic aperture radar (SAR) imagery requires increased understanding of processes that change the state of the sea surface. Wind stress that results from kilometer-scale boundary layer circulations produces sea-surface stress patterns responsible for some of this sea surface variability. A Galerkin model of these boundary layer circulations—that take the form of two-dimensional rolls and three-dimensional convective cells—is developed here to study their effect on sea surface stress.

The objectives of previous investigations using spectral models were focused on the structure of the circulations in the middle levels of the boundary layer, and so for simplicity the stress and heat flux were assumed to vanish at the lower boundary. However these boundary conditions do not allow the study of stress variability at the sea surface. The goal of this thesis is to create a marine atmospheric boundary layer model that allows nonzero heat and momentum fluxes at the lower boundary. Surface layer similarity theory is used to specify constant forcing parameter values in the lower boundary conditions. The focus of this study is to determine whether these lower boundary conditions allow the model to capture the behavior of the roll circulations and, if they do, to determine the fluxes at the lower boundary that influence kilometer-scale sea stress variability.

Case study results demonstrate that the model does indeed capture the spatial organization of the roll circulations and does correctly reproduce the vertical profiles of heat and momentum flux. The results also show that the temperature perturbation is a maximum at the lower boundary where the primary heat source is located. The temporal periodicity of the system is consistent with physical and numerical analyses as well.

However there are two distinct case study results that indicate further redesign of the model is needed before the surface stress patterns can be studied. The first result is that only an amplifying roll solution could be found, indicating that a source of energy is not being damped properly. The other result is that the maximum vertical velocity magnitude occurs at the lower boundary, which produces a profile that is not consistent with observations.

The case study results point to the need to re-evaluate the use of surface layer similarity theory for obtaining the parameter values in the new boundary conditions. For example, because the roll circulations scale with the boundary layer depth, it seems likely that convective scaling theory might produce more appropriate lower boundary conditions than would surface layer theory.

## REFERENCES

- Brown, R. A., 1980: Longitudinal instabilities and secondary flows in the planetary boundary layer: A review. *Rev. Geophys. Space Phys.*, **18**, 683-697.
- Brümmer, B. and B. Busack, 1990: Convective patterns within a field of stratocumulus. *Mon. Wea. Rev.*, **118**, 801-817.
- Gerling, T. W., 1985: Remote sensing of the ocean-surface wind field with a scatterometer and a synthetic aperture radar. *John Hopkins APL Digest*, **6**, 320-329.
- Gerling, T. W., 1986: Structure of the surface wind field from the Seasat SAR. *J. Geophys. Res.*, **91**, 2308-2320.
- Haack, T. and H. N. Shirer, 1992: Mixed convective-dynamic roll vortices and their effects on initial wind and temperature profiles. *J. Atmos. Sci.*, **49**, 1181-1201.
- Higgins, R. W., 1987: From the equations of motion to spectral models. *Nonlinear Hydrodynamic Modeling: A Mathematical Introduction. Lecture Notes in Physics*, **271**, H. N. Shirer, Ed., Springer-Verlag, 47-69.
- Laufersweiler, M. J. and H. N. Shirer, 1989: A simple dynamical model of a stratocumulus-topped boundary layer. *J. Atmos. Sci.*, **46**, 1133-1153.
- Lilly, D. K., 1966: On the instability of Ekman boundary flow. *J. Atmos. Sci.*, **23**, 481-494.
- Pyle, R. J., 1987: Typical branching forms: Periodic solutions. *Nonlinear Hydrodynamic Modeling: A Mathematical Introduction. Lecture Notes in Physics*, **271**, H. N. Shirer, Ed., Springer-Verlag, 264-291.
- Schmidt, H. and U. Schumann, 1989: Coherent structure of the convective boundary layer derived from large-eddy simulations. *J. Fluid Mech.*, **200**, 511-562.
- Shirer, H. N., 1986: On cloud street development in three dimensions: Parallel and Rayleigh instabilities. *Contrib. Atmos. Phys.*, **59**, 126-149.
- Shirer, H. N., Ed., 1987: *Nonlinear Hydrodynamic Modeling: A Mathematical Introduction. Lecture Notes in Physics*, **271**, Springer-Verlag, 546 pp.

Stensrud, D. J., 1987: The expected branching solution: Preferred wavelengths and orientations. *Nonlinear Hydrodynamic Modeling: A Mathematical Introduction. Lecture Notes in Physics*, **271**, H. N. Shirer, Ed., Springer-Verlag, 292-324.

Stensrud, D. J. and H. N. Shirer, 1988: Development of boundary layer rolls from dynamic instabilities. *J. Atmos. Sci.*, **45**, 1007-1019.

Stull, R. B., 1988: *An Introduction to Boundary Layer Meteorology*. Kluwer Academic Publishers, Boston, 666 pp.

Visecky, J. F. and R. H. Stewart, 1982: The observation of ocean surface phenomena using imagery from the SEASAT synthetic aperture radar: An assessment. *J. Geophys. Res.*, **87**, 3397-3430.

## ABSTRACT

The interpretation of satellite- or aircraft-borne synthetic aperture radar (SAR) imagery requires increased understanding of processes that change the state of the sea surface. Wind stress that results from kilometer-scale boundary layer circulations produces sea-surface stress patterns responsible for some of this sea surface variability. A Galerkin model of these boundary layer circulations—that take the form of two-dimensional rolls and three-dimensional convective cells—is developed here to study their effect on sea surface stress.

The objectives of previous investigations using spectral models were focused on the structure of the circulations in the middle levels of the boundary layer, and so for simplicity the stress and heat flux were assumed to vanish at the lower boundary. However these boundary conditions do not allow the study of stress variability at the sea surface. The goal of this thesis is to create a marine atmospheric boundary layer model that allows nonzero heat and momentum fluxes at the lower boundary. Surface layer similarity theory is used to specify constant forcing parameter values in the lower boundary conditions. The focus of this study is to determine whether these lower boundary conditions allow the model to capture the behavior of the roll circulations and, if they do, to determine the fluxes at the lower boundary that influence kilometer-scale sea stress variability.

Case study results demonstrate that the model does indeed capture the spatial organization of the roll circulations and does correctly reproduce the vertical profiles of heat and momentum flux. The results also show that the temperature perturbation is a maximum at the lower boundary where the primary heat source is located. The temporal periodicity of the system is consistent with physical and numerical analyses as well.

However there are two distinct case study results that indicate further redesign of the model is needed before the surface stress patterns can be studied. The first result is that only an amplifying roll solution could be found, indicating that a source of energy is not being damped properly. The other result is that the maximum vertical velocity magnitude occurs at the lower boundary, which produces a profile that is not consistent with observations.

The case study results point to the need to re-evaluate the use of surface layer similarity theory for obtaining the parameter values in the new boundary conditions. For example, because the roll circulations scale with the boundary layer depth, it seems likely that convective scaling theory might produce more appropriate lower boundary conditions than would surface layer theory.

## REFERENCES

- Brown, R. A., 1980: Longitudinal instabilities and secondary flows in the planetary boundary layer: A review. *Rev. Geophys. Space Phys.*, **18**, 683-697.
- Brümmer, B. and B. Busack, 1990: Convective patterns within a field of stratocumulus. *Mon. Wea. Rev.*, **118**, 801-817.
- Gerling, T. W., 1985: Remote sensing of the ocean-surface wind field with a scatterometer and a synthetic aperture radar. *John Hopkins APL Digest*, **6**, 320-329.
- Gerling, T. W., 1986: Structure of the surface wind field from the Seasat SAR. *J. Geophys. Res.*, **91**, 2308-2320.
- Haack, T. and H. N. Shirer, 1992: Mixed convective-dynamic roll vortices and their effects on initial wind and temperature profiles. *J. Atmos. Sci.*, **49**, 1181-1201.
- Higgins, R. W., 1987: From the equations of motion to spectral models. *Nonlinear Hydrodynamic Modeling: A Mathematical Introduction. Lecture Notes in Physics*, **271**, H. N. Shirer, Ed., Springer-Verlag, 47-69.
- Laufersweiler, M. J. and H. N. Shirer, 1989: A simple dynamical model of a stratocumulus-topped boundary layer. *J. Atmos. Sci.*, **46**, 1133-1153.
- Lilly, D. K., 1966: On the instability of Ekman boundary flow. *J. Atmos. Sci.*, **23**, 481-494.
- Pyle, R. J., 1987: Typical branching forms: Periodic solutions. *Nonlinear Hydrodynamic Modeling: A Mathematical Introduction. Lecture Notes in Physics*, **271**, H. N. Shirer, Ed., Springer-Verlag, 264-291.
- Schmidt, H. and U. Schumann, 1989: Coherent structure of the convective boundary layer derived from large-eddy simulations. *J. Fluid Mech.*, **200**, 511-562.
- Shirer, H. N., 1986: On cloud street development in three dimensions: Parallel and Rayleigh instabilities. *Contrib. Atmos. Phys.*, **59**, 126-149.
- Shirer, H. N., Ed., 1987: *Nonlinear Hydrodynamic Modeling: A Mathematical Introduction. Lecture Notes in Physics*, **271**, Springer-Verlag, 546 pp.

Stensrud, D. J., 1987: The expected branching solution: Preferred wavelengths and orientations. *Nonlinear Hydrodynamic Modeling: A Mathematical Introduction. Lecture Notes in Physics*, **271**, H. N. Shirer, Ed., Springer-Verlag, 292-324.

Stensrud, D. J. and H. N. Shirer, 1988: Development of boundary layer rolls from dynamic instabilities. *J. Atmos. Sci.*, **45**, 1007-1019.

Stull, R. B., 1988: *An Introduction to Boundary Layer Meteorology*. Kluwer Academic Publishers, Boston, 666 pp.

Visecky, J. F. and R. H. Stewart, 1982: The observation of ocean surface phenomena using imagery from the SEASAT synthetic aperture radar: An assessment. *J. Geophys. Res.*, **87**, 3397-3430.

The Pennsylvania State University

The Graduate School

Department of Meteorology

MODELING SEA-SURFACE STRESS VARIABILITY  
CAUSED BY KILOMETER-SCALE  
MARINE ATMOSPHERIC BOUNDARY LAYER CIRCULATIONS

A Thesis in  
Meteorology

by  
Louis Vincent Zuccarello

Submitted in Partial Fulfillment  
of the Requirements  
for the Degree of

Master of Science

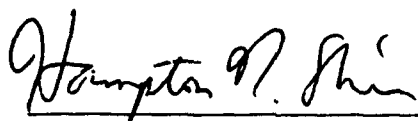
May 1994

I grant The Pennsylvania State University the nonexclusive right to use this work for the University's own purposes and to make single copies of the work available to the public on a not-for-profit basis if copies are not otherwise available.

Louis Vincent Zuccarello  
Louis Vincent Zuccarello

We approve the thesis of Louis Vincent Zuccarello.

Date of Signature



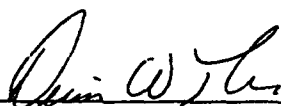
Hampton N. Shirer  
Associate Professor of Meteorology  
Thesis Adviser

16 March 1994



Robert Wells  
Professor of Mathematics

16 March 1994



Dennis W. Thomson  
Professor of Meteorology  
Head of the Department of Meteorology

16 March 94

## ABSTRACT

The interpretation of satellite- or aircraft-borne synthetic aperture radar (SAR) imagery requires increased understanding of processes that change the state of the sea surface. Wind stress that results from kilometer-scale boundary layer circulations produces sea-surface stress patterns responsible for some of this sea surface variability. A Galerkin model of these boundary layer circulations—that take the form of two-dimensional rolls and three-dimensional convective cells—is developed here to study their effect on sea surface stress.

The objectives of previous investigations using spectral models were focused on the structure of the circulations in the middle levels of the boundary layer, and so for simplicity the stress and heat flux were assumed to vanish at the lower boundary. However these boundary conditions do not allow the study of stress variability at the sea surface. The goal of this thesis is to create a marine atmospheric boundary layer model that allows nonzero heat and momentum fluxes at the lower boundary. Surface layer similarity theory is used to specify constant forcing parameter values in the lower boundary conditions. The focus of this study is to determine whether these lower boundary conditions allow the model to capture the behavior of the roll circulations and, if they do, to determine the fluxes at the lower boundary that influence kilometer-scale sea stress variability.

Case study results demonstrate that the model does indeed capture the spatial organization of the roll circulations and does correctly reproduce the vertical profiles of heat and momentum flux. The results also show that the temperature perturbation is a maximum at the lower boundary where the primary heat source is located. The temporal periodicity of the system is consistent with physical and numerical analyses as well.

However there are two distinct case study results that indicate further redesign of the model is needed before the surface stress patterns can be studied. The first result is that only an amplifying roll solution could be found, indicating that a source of energy is not being damped properly. The other result is that the maximum vertical velocity magnitude occurs at the lower boundary, which produces a profile that is not consistent with observations.

The case study results point to the need to re-evaluate the use of surface layer similarity theory for obtaining the parameter values in the new boundary conditions. For example, because the roll circulations scale with the boundary layer depth, it seems likely that convective scaling theory might produce more appropriate lower boundary conditions than would surface layer theory.

## TABLE OF CONTENTS

LIST OF FIGURES . . . . .	vi
LIST OF TABLES . . . . .	viii
ACKNOWLEDGMENTS . . . . .	ix
Chapter 1. INTRODUCTION . . . . .	1
Chapter 2. MODEL DEVELOPMENT . . . . .	4
2.1. The Partial Differential Equations . . . . .	6
2.2. The Spectral System . . . . .	11
2.3. The Computer Model . . . . .	18
Chapter 3. MODEL EVALUATION. . . . .	21
3.1. Parameter Values and Initial Conditions. . . . .	21
3.2. Case Study . . . . .	31
Chapter 4. CONCLUSIONS . . . . .	46
REFERENCES . . . . .	50
Appendix A. DETERMINING THE CONSTANTS IN THE BOUNDARY CONDITIONS . . . . .	52
Appendix B. VERTICAL BASIS FUNCTIONS AND EIGENVALUES . . .	58

## LIST OF FIGURES

2.1	A schematic cross-section of the model domain in the x-z plane . . .	5
2.2	A schematic cross-section of the model domain in the y-z plane . . .	5
3.1	Temperature vertical basis function profiles for the four wavenumbers chosen . . . . .	25
3.2	Velocity vertical basis function (vertical velocity) profiles for the four wavenumbers chosen . . . . .	26
3.3	The square root of the sum of the squares for the 60 time-dependent amplitude coefficients, demonstrating that the system is approaching a state of quasi-equilibration . . . . .	29
3.4	Time series of one of the time-dependent temperature amplitude coefficients ( $T_{11}$ ), demonstrating that the bifurcating solution has a period of approximately 9.3 minutes . . . . .	32
3.5	Time series of one of the time-dependent velocity amplitude coefficients ( $\psi_{11}$ ), demonstrating that the bifurcating solution has a period of approximately 9.3 minutes . . . . .	33
3.6	Planview of vertical velocity $w^*$ in the dimensionless coordinate system at the height $h_{LB}$ of the lower boundary . . . . .	34
3.7	Planview of vertical heat flux $w^*T^*$ in the dimensionless coordinate system at the height $h_{LB}$ of the lower boundary . . . . .	36
3.8	Vertical heat flux $w^*T^*$ profile integrated over the dimensionless horizontal plane . . . . .	37
3.9	Modification of the vertical temperature profile by the rolls . . . . .	39
3.10	Profile of vertical flux of westerly momentum given by integration of $u^*w^*$ over the dimensionless horizontal plane. . . . .	40

3.11	Profile of vertical flux of southerly momentum given by integration of $v^*w^*$ over the dimensionless horizontal plane . . . . .	41
3.12	Vertical profile for the perturbation velocity component $u^*$ found by integrating as in Fig. 3.10 . . . . .	42
3.13	Vertical profile for the perturbation velocity component $v^*$ found by integrating as in Fig. 3.10 . . . . .	44
3.14	Vertical velocity profile for the center of an updraft . . . . .	45

## LIST OF TABLES

3.1	Parameter values used in the model . . . . .	22
3.2	Parameter values for surface layer $\Delta T$ and associated calculated values for $z_s$ , $L$ , $s_m$ , and $s_T$ . . . . .	23
3.3	Case study values for $\omega_j$ and $\varpi_q$ for $j = q = 1, 2, 3, 4$ . . . . .	24

## ACKNOWLEDGMENTS

The research presented in this thesis was sponsored by the Office of Naval Research through grant N00014-90-J-4012. The financial support for my academic program was provided by the Air Force Institute of Technology (AFIT) Civilian Institution Program.

There are many people responsible for making this project an interesting and fruitful endeavor. Ms. Julie L. Schramm did much of the background work needed to implement this model. She developed the boundary conditions I used and provided computer programs that allowed me to incorporate the boundary conditions into my model. The subroutine supplied by Dr. George S. Young, which was implemented by Mr. Dave V. Ledvina based on work done by Dr. Chris W. Fairall, was crucial to Julie's development of the boundary conditions. Dr. Young also played an important role in interpreting my results and offering many useful suggestions for further research. Mr. Peter J. Bromfield, Dr. Mark J. Laufersweiler, and Dr. Harry W. Henderson provided valuable computer and meteorological expertise. I also wish to thank my AFIT colleagues for their help and camaraderie.

Dr. Hampton N. Shirer and Dr. Robert Wells are the two individuals who really made the completion of this work possible. They both gave selflessly of their time and always answered my many questions. Dr. Wells provided the mathematical insight that was crucial to the development of this innovative model. I thank him for his support and encouragement. Dr. Shirer, thesis adviser, gave me the opportunity to work on this project. He has proved to be an outstanding adviser, teacher, and friend. Dr. Shirer's professionalism and meteorological expertise have made working with him a real honor. I thank him for his tireless efforts and hope to work with him again.

Finally, I wish to give special thanks to my wife Lisa who has been a constant source of love and support. Her understanding and the birth of our daughter Veronica have made the completion of my M.S. degree during the past 21 months very rewarding.

## Chapter 1

### INTRODUCTION

The use of satellite- or aircraft-borne synthetic aperture radars (SAR) as meteorological and oceanographic observation systems holds great promise (Visecky and Stewart 1982). Unfortunately, the interpretation of SAR signals is greatly dependent upon the nature of the constantly changing state of the sea surface. The dominant atmospheric mechanism for forcing the sea surface is wind stress, and so a better understanding of the effects of this stress is required for us to be able to interpret correctly the SAR signals. One approach is to use atmospheric modeling of boundary layer flow to analyze how it might modulate sea-surface stress patterns.

We focus our study on kilometer-scale marine atmospheric boundary layer circulations. There are two types of kilometer-scale circulations that affect sea-surface stress. The first type comprises quasi-two-dimensional boundary layer rolls. Evidence from SAR imagery of stress patterns caused by roll circulations is well documented, for example, by Gerling (1985, 1986). The second type comprises convective cells, which are fully three-dimensional flows that may form independently of the rolls in less windy conditions. Such cells may also evolve from two-dimensional rolls as the forcing rates increase. As described extensively elsewhere (e.g. Brown 1980; Stensrud 1987), each of these boundary layer circulations may be driven by both convective and dynamic instability mechanisms. Some important mechanisms include boundary layer wind shear, air/sea temperature difference, and the magnitude of heating effects in clouds. All of these mechanisms are ultimately responsible for the downward transport of horizontal momentum that produces stress variability at the sea surface.

A number of nonlinear modeling studies of boundary layer rolls (Shirer 1986; Stensrud and Shirer 1988; Laufersweiler and Shirer 1989; Haack and Shirer 1992) have sought to identify the dominant forcing mechanisms and characteristic spatial and temporal responses of these convective boundary layer circulations. These nonlinear, Galerkin models, which are based on the Boussinesq system of equations and use sinusoidal basis functions, provide wind profile modifications, preferred orientation angles and wavelengths, and simplicity in the study of bifurcation and stability properties. These models also yield profiles of the vertical fluxes of horizontal momentum and heat.

The objectives of the above studies are focused on determining the structure of the circulations in the middle levels of the boundary layer, and so for simplicity the stress and heat flux are assumed to vanish at the lower boundary. However, these boundary conditions cannot allow us to study the stress variability at the sea surface, unless bulk aerodynamic techniques are used (Stull 1988). Thus the goal of this thesis is to create a nonlinear, Boussinesq, three-dimensional boundary layer model that allows nonzero heat and momentum fluxes at the lower boundary. There are a number of approaches that might be adopted to determine appropriate lower boundary conditions. For example, Schmidt and Schumann (1989) used surface layer similarity theory to specify the lower boundary conditions in their model, which they used to successfully capture kilometer-scale boundary layer structures.

We also use similarity theory, but adopt a different approach to specify our boundary conditions. We set the bottom of our domain at 10 *m* above the sea surface and then choose lower boundary conditions that represent wind and temperature values typically observed at this height in the surface layer. To test this approach, we use empirically derived similarity relationships for an unstable environment (Stull 1988). These relationships lead to constant forcing parameters that may be used to specify the

lower boundary conditions. These boundary conditions allow for a more realistic incorporation of thermal forcing, which in earlier models is spread throughout the entire vertical domain via the Rayleigh number  $Ra$ . In reality, the thermal forcing at the lower boundary should drive the system and the value of the traditional Rayleigh number should be inferred from the model solutions. Finally, and for simplicity, the upper boundary conditions are taken to be rigid, stress-free, and perfectly conducting as in the earlier models.

We then develop the vertical basis functions for the model expansions by solving a more realistic eigenfunction problem based on the new boundary conditions. These basis functions are expressed in terms of exponential and trigonometric functions. When we create the spectral model, products of these basis functions must be integrated; we obtain expressions for these integrals using the symbolic manipulator software DERIVE. These results are then incorporated into the FORTRAN program that does the numerical integration of the model and subsequent simulation of the boundary layer circulations.

The focus of this study is to determine whether the lower boundary conditions specified using similarity theory do, in fact, allow the model to capture the behavior of the roll circulations and, if they do, to determine the fluxes at the lower boundary that influence kilometer-scale sea stress variability. In Chapter 2, we explain the development of the 60-coefficient nonlinear dynamic model, which is still much smaller than a Large Eddy Simulation (LES) model, and so, in principle, can be studied more completely. We first determine the appropriate partial differential system of equations, next form the spectral system, and finally describe the computer model. In Chapter 3, we present the results of some model integrations, first specifying the appropriate model parameter values and initial conditions and then analyzing the data. Finally, in Chapter 4, we evaluate these model results and suggest areas for further analysis and study.

## Chapter 2

### MODEL DEVELOPMENT

The convective nature of boundary layer roll, or secondary, circulations allows us to choose a set of approximate equations in which certain terms from the complete set of equations are neglected. These approximate equations form what is known as the shallow Boussinesq system. The roll circulations are represented by perturbations superimposed on a basic state that is time-independent, isopycnic, hydrostatic, and horizontally moving (Shirer 1986). We assume that the perturbations possess a three-dimensional structure, and so we must consider both roll-perpendicular and roll-parallel variations. The horizontal domain is infinite and cyclically continuous at  $x = 0, y = 0$  and  $x = L_x, y = L_y$ , where  $L_x$  and  $L_y$  are the roll wavelength components. The vertical domain ranges from  $z = h_{LB}$  to  $z = z_T$ , where  $h_{LB}$  is the height of the lower boundary and  $z_T$  is the cloud top height or inversion base. Only the part of the circulation above  $h_{LB}$  is specifically modeled; the part below  $h_{LB}$  is parameterized with surface layer similarity theory. In dimensionless form the domain is defined by  $0 \leq x^* \leq 1$ ,  $0 \leq y^* \leq 1$ , and  $0 \leq z^* \leq 1$ . A schematic representation of the domain is given in Figs. 2.1-2.2.

The basic state, known as the conductive state and denoted by subscript  $o$ , is given as

$$\mathbf{v}_o = U(z)\mathbf{i} + V(z)\mathbf{j} \quad (2.1)$$

$$\rho_o = \rho_\infty \quad (2.2)$$

$$T_o(z) = T_\infty - \Delta_z T(z/z_T) \quad (2.3)$$

$$p_o(z) = p_\infty - \rho_\infty g z, \quad (2.4)$$

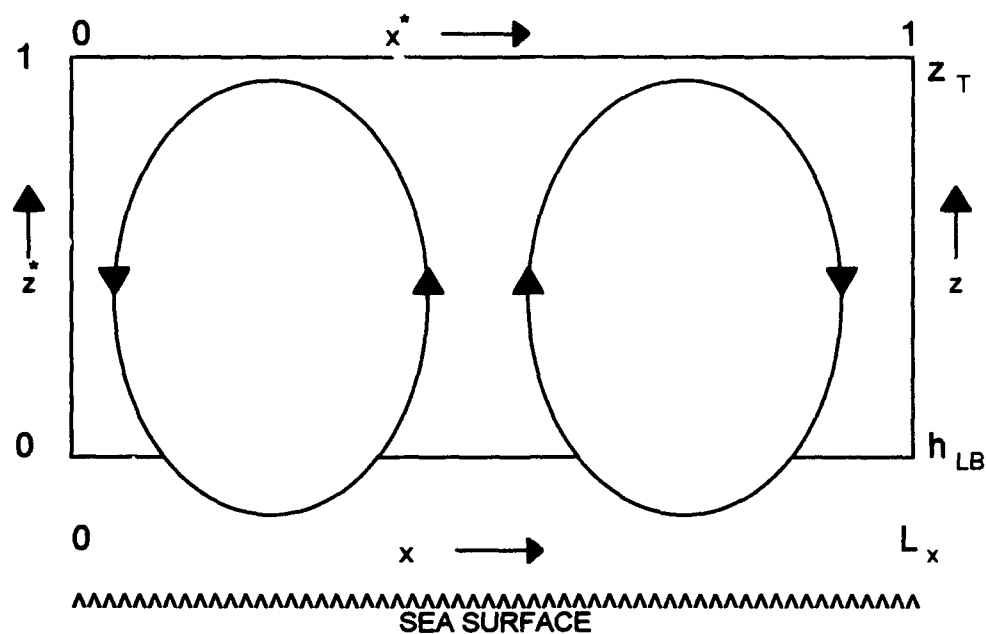


Fig. 2.1. A schematic cross-section of the model domain in the  $x$ - $z$  plane.

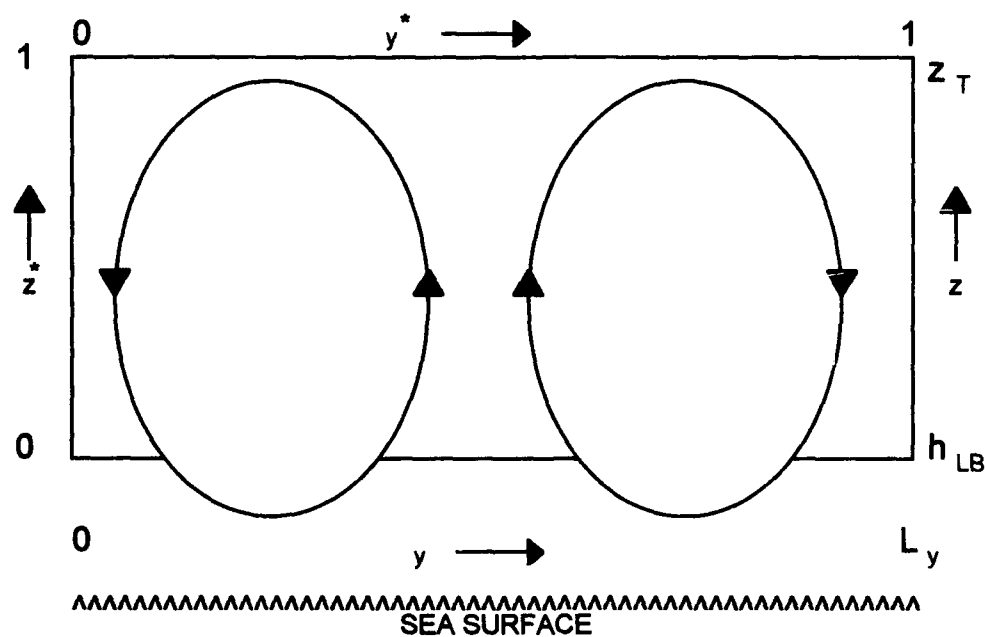


Fig. 2.2. A schematic cross-section of the model domain in the  $y$ - $z$  plane.

where subscript  $\infty$  denotes the value at the lower boundary,  $U(z)$  and  $V(z)$  are the components of the mean horizontal wind, and  $\Delta_z T$  is a constant lapse rate defined as the temperature difference between the lower and upper boundaries. The three-dimensional secondary circulation, denoted by primes, is given by

$$u'(x, y, z, t) = u(x, y, z, t) - U(z) \quad (2.5)$$

$$v'(x, y, z, t) = v(x, y, z, t) - V(z) \quad (2.6)$$

$$w'(x, y, z, t) = w(x, y, z, t) \quad (2.7)$$

$$\rho'(x, y, z, t) = \rho(x, y, z, t) - \rho_\infty \quad (2.8)$$

$$T'(x, y, z, t) = T(x, y, z, t) - T_\infty(z) \quad (2.9)$$

$$p'(x, y, z, t) = p(x, y, z, t) - p_\infty(z). \quad (2.10)$$

In the Boussinesq system, compression is considered negligible. Other approximations include writing the equation of state in a normalized form and linearizing the pressure gradient force (Shirer 1987).

## 2.1. The Partial Differential Equations

The Boussinesq system of equations for the perturbation temperature  $T'$  and the perturbation velocity vector  $\mathbf{v}'$  takes the form (e.g. Shirer 1986)

$$\frac{\partial T'}{\partial t} + \mathbf{V} \cdot \nabla T' + \mathbf{v}' \cdot \nabla T' = \frac{\Delta_z T}{z_T} w' + \kappa \nabla^2 T' - \sigma \nabla^4 T' \quad (2.11)$$

$$\frac{\partial \mathbf{v}'}{\partial t} + \mathbf{V} \cdot \nabla \mathbf{v}' + w' \frac{\partial \mathbf{V}}{\partial z} + \mathbf{v}' \cdot \nabla \mathbf{v}' = -\frac{1}{\rho_\infty} \nabla p' - f \mathbf{k} \times \mathbf{v}' + g \frac{T'}{T_\infty} \mathbf{k} + \nu \nabla^2 \mathbf{v}' - \varepsilon \nabla^4 \mathbf{v}' \quad (2.12)$$

$$\nabla \bullet \mathbf{v}' = 0, \quad (2.13)$$

where  $\kappa$  is the constant eddy thermometric conductivity and  $\nu$  is the constant eddy viscosity. We have added additional terms to (2.11)-(2.12) with dissipation parameters  $\sigma$  and  $\varepsilon$  to control the growth of any numerical instabilities. A dimensionless form of the equations is used based on the definitions

$$\mathbf{v}'_H = (u^* \mathbf{i} + v^* \mathbf{j}) \frac{\kappa}{z_T - h_{LB}} \quad (2.14)$$

$$w' = \frac{w^* \kappa}{z_T - h_{LB}} \quad (2.15)$$

$$x = x^* L_x \quad (2.16)$$

$$y = y^* L_y \quad (2.17)$$

$$z = z^* (z_T - h_{LB}) + h_{LB} \quad (2.18)$$

$$t = t^* \frac{(z_T - h_{LB})^2}{\kappa} \quad (2.19)$$

$$T' = \frac{T^* \nu \kappa T_\infty}{g(z_T - h_{LB})^3} \quad (2.20)$$

$$p' = \frac{p^* \rho_\infty \kappa^2}{(z_T - h_{LB}) L_x} \quad (2.21)$$

$$U(z) = |\mathbf{V}(z_T)| U^*(z^*) \quad (2.22)$$

$$V(z) = |\mathbf{V}(z_T)| V^*(z^*) \quad (2.23)$$

$$f = \frac{f^* \kappa}{(z_T - h_{LB})^2} \quad (2.24)$$

These dimensionless equations take the form

$$\frac{\partial T^*}{\partial t^*} = \tilde{\nabla}^2 T^* - \beta \tilde{\nabla}^4 T^* - \text{Re } \mathbf{V}^* \cdot \tilde{\nabla} T^* + \text{Raw}^* - \mathbf{v}^* \cdot \tilde{\nabla} T^* \quad (2.25)$$

$$\begin{aligned} \frac{\partial \mathbf{v}^*}{\partial t^*} = & -a_x \tilde{\nabla} p^* + P \tilde{\nabla}^2 \mathbf{v}^* - \mu \tilde{\nabla}^4 \mathbf{v}^* - f^* P \mathbf{k} \times \mathbf{v}^* + P T^* \mathbf{k} \\ & - (\text{Re } \mathbf{V}^* + \mathbf{v}^*) \cdot \tilde{\nabla} \mathbf{v}^* - \text{Re } w^* \frac{\partial \mathbf{V}^*}{\partial z^*}, \end{aligned} \quad (2.26)$$

where

$$\tilde{\nabla} = a_x \frac{\partial}{\partial x^*} \mathbf{i} + a_y \frac{\partial}{\partial y^*} \mathbf{j} + \frac{\partial}{\partial z^*} \mathbf{k}. \quad (2.27)$$

The parameter  $\beta$  is the dimensionless version of  $\sigma$  and the parameter  $\mu$  is the dimensionless version of  $\varepsilon$ . The values of the dimensionless parameters  $\beta$  and  $\mu$  control the magnitude of the numerical dissipation terms. The dimensionless forms lead to two forcing parameters in (2.25)-(2.26). The Reynolds number  $\text{Re}$  is given by

$$\text{Re} = |\mathbf{V}(z_T)| (z_T - h_{LB}) / \kappa \quad (2.28)$$

and represents dynamic forcing by the mean wind shear of the basic state. The Rayleigh

number  $Ra$  is given by

$$Ra = \frac{g\Delta_z T(z_T - h_{LB})^3}{\nu\kappa T_\infty} \quad (2.29)$$

and represents thermodynamic forcing across the domain.

Three other dimensionless variables appear in the system. The eddy Prandtl number is defined as

$$P = \nu/\kappa. \quad (2.30)$$

The roll aspect ratios,  $a_x$  and  $a_y$ , are defined as

$$a_x = \frac{(z_T - h_{LB})}{L_x} \quad (2.31)$$

$$a_y = \frac{(z_T - h_{LB})}{L_y}. \quad (2.32)$$

The vector  $\mathbf{V}^*(z^*)$  represents the dimensionless mean wind profile. As a result of the definitions (2.22)-(2.23), it follows immediately that  $|\mathbf{V}^*(1)| = 1$ .

We further transform the momentum equation (2.26) by taking the curl to form a

vorticity equation, thereby eliminating pressure. The resulting equation is

$$\begin{aligned} \frac{\partial(\tilde{\nabla} \times \mathbf{v}^*)}{\partial t^*} = & P\tilde{\nabla}^2(\tilde{\nabla} \times \mathbf{v}^*) - \mu\tilde{\nabla}^4(\tilde{\nabla} \times \mathbf{v}^*) - f^*P[\tilde{\nabla} \times (\mathbf{k} \times \mathbf{v}^*)] + P(\tilde{\nabla} \times T^*\mathbf{k}) \\ & - \text{Re}[\tilde{\nabla} \times (\mathbf{V}^* \bullet \tilde{\nabla} \mathbf{v}^*)] - \text{Re}\left[\tilde{\nabla} \times \left(w^* \frac{\partial \mathbf{V}^*}{\partial z^*}\right)\right] - [\tilde{\nabla} \times (\mathbf{v}^* \bullet \tilde{\nabla} \mathbf{v}^*)]. \end{aligned} \quad (2.33)$$

In order to solve the system of equations (2.25) and (2.33), we must specify appropriate boundary conditions. For simplicity, the lateral boundaries are cyclic, and the upper vertical boundary is rigid, stress-free, and perfectly conducting. In contrast, an important source of energy for the circulations exists at the lower boundary; there boundary conditions are specified using surface layer similarity theory as described in Appendix A. The vertical boundary conditions are summarized below for  $s_r > 0$  and  $s_m > 0$ :

$$T^*(0) + s_r \frac{\partial T^*(0)}{\partial z^*} = 0 \quad (2.34)$$

$$u^*(0) - s_m \frac{\partial u^*(0)}{\partial z^*} = 0 \quad (2.35)$$

$$v^*(0) - s_m \frac{\partial v^*(0)}{\partial z^*} = 0 \quad (2.36)$$

$$\frac{\partial w^*(0)}{\partial z^*} - s_m \frac{\partial^2 w^*(0)}{\partial z^{*2}} = 0 \quad (2.37)$$

$$T^*(1) = 0 \quad (2.38)$$

$$\frac{\partial u^*(1)}{\partial z^*} = \frac{\partial v^*(1)}{\partial z^*} = w^*(1) = 0, \quad (2.39)$$

where  $s_m$ , the Schramm momentum constant, and  $s_T$ , the Schramm temperature constant, which are both defined in Appendix A, control the forcing at the lower vertical boundary.

## 2.2. The Spectral System

The next step in the development of the model is to create an appropriate system of ordinary differential equations from the partial differential system given in the previous section. We use the Galerkin technique or spectral method to form this spectral model. First, we substitute the Fourier expansions for the dependent variables into the appropriate partial differential equation. Next, we multiply the resulting equation by the particular eigenfunction that the amplitude coefficient multiplies in the expansion. We then integrate the result over the spatial domain, using, where possible, orthogonality of the eigenfunctions in the expansion. Finally, we retain only those terms that are nonzero (Higgins 1987).

Owing to the complexity of the model, the above steps are performed separately for each term in the partial differential equations, with the results being stored in an appropriate matrix. The truncation chosen, which is listed below, results in a system of 60 equations, 20 in temperature and 40 in velocity. Each term in each equation may be represented by a  $60 \times 60$  matrix that is multiplied by a 60-element vector representing the 60 amplitude coefficients. The resulting system takes the form

$$A\dot{y} = By + C(y)y, \quad (2.40)$$

where  $A$  is a  $60 \times 60$  matrix of inner products multiplying the 60-element vector  $\dot{y}$  that contains the temporal derivatives of the amplitude coefficients,  $B$  is a  $60 \times 60$  constant matrix, based on the linear terms of the partial differential equations, multiplying the 60-element vector  $y$  that contains the amplitude coefficients, and  $C$  is a  $60 \times 60$   $y$ -dependent linear matrix, based on the advective terms of the partial differential equations, multiplying the same 60-element vector. Because  $A$  is invertible, we are then able to solve for the time-dependent amplitude coefficients by numerically integrating the following system:

$$\dot{y} = A^{-1}By + A^{-1}C(y)y. \quad (2.41)$$

To find (2.40) from (2.25) and (2.33), we first choose a truncated Fourier expansion for the dependent variable  $T^*$  composed of temporally dependent amplitudes, spatially dependent trigonometric functions with horizontal wavenumbers  $l$  and  $m$ , and vertical basis functions:

$$T^*(x^*, y^*, z^*, t^*) = \sum_{i=0}^4 \sum_{j=1}^4 T_{ij}(t^*) \text{trig}_i(x^*, y^*) F_j(z^*), \quad (2.42)$$

where

$$\text{trig}_0(x^*, y^*) = 1 \quad (2.43)$$

$$\text{trig}_1(x^*, y^*) = \sin 2\pi x^* \sin 2\pi y^* \quad (2.44)$$

$$\text{trig}_2(x^*, y^*) = \sin 2\pi x^* \cos 2\pi y^* \quad (2.45)$$

$$\text{trig}_3(x^*, y^*) = \cos 2\pi x^* \sin 2\pi y^* \quad (2.46)$$

$$\text{trig}_4(x^*, y^*) = \cos 2\pi x^* \cos 2\pi y^* \quad (2.47)$$

$$F_1(z^*) = \cosh \omega_1 z^* - \frac{1}{s_T \omega_1} \sinh \omega_1 z^* \quad \text{for } s_T < 1 \quad (2.48)$$

$$F_1(z^*) = \cos \omega_1 z^* - \frac{1}{s_T \omega_1} \sin \omega_1 z^* \quad \text{for } s_T > 1 \quad (2.49)$$

$$s_T \omega_1 = \tanh \omega_1 \quad \text{for } s_T < 1 \quad (2.50)$$

$$s_T \omega_1 = \tan \omega_1 \quad \text{for } s_T > 1 \quad (2.51)$$

$$F_j(z^*) = \cos \omega_j z^* - \frac{1}{s_T \omega_j} \sin \omega_j z^* \quad \text{for } j = 2, 3, 4 \quad (2.52)$$

$$s_T \omega_j = \tan \omega_j \quad \text{for } j = 2, 3, 4, \quad (2.53)$$

and the vertical basis functions are orthogonal. A complete discussion of the vertical basis functions and associated eigenvalues is found in Appendix B.

We next must choose an expansion for the velocity vector  $\mathbf{v}^*$ . Because it is nondivergent, it will be convenient to represent  $\mathbf{v}^*$  (nonuniquely) as the curl of a vector streamfunction  $\mathbf{A}^*$  that is the sum of two vector streamfunctions  $\boldsymbol{\psi}^*$  and  $\boldsymbol{\eta}^*$ . Therefore, the velocity perturbation vector  $\mathbf{v}^*$  may be expressed as

$$\mathbf{v}^* = \nabla \times \mathbf{A}^* = \nabla \times \boldsymbol{\psi}^* + \nabla \times \boldsymbol{\eta}^*. \quad (2.54)$$

We then substitute this new definition for  $\mathbf{v}^*$  into the partial differential system (2.25) and (2.33). We can now use a truncated Fourier expansion to represent the dependent vector

streamfunctions  $\psi^*$  and  $\eta^*$ :

$$\psi^*(x^*, y^*, z^*, t^*) = \sum_{p=0}^4 \sum_{q=1}^4 \psi_{pq}(t^*) \text{trig}_p(x^*, y^*) h_q(z^*) \mathbf{i} + 0\mathbf{j} + 0\mathbf{k} \quad (2.55)$$

$$\eta^*(x^*, y^*, z^*, t^*) = 0\mathbf{i} + \sum_{p=0}^4 \sum_{q=1}^4 \eta_{pq}(t^*) \text{trig}_p(x^*, y^*) h_q(z^*) \mathbf{j} + 0\mathbf{k}, \quad (2.56)$$

where  $\text{trig}_p(x^*, y^*)$  is defined as in (2.43)–(2.47), and

$$h_q(z^*) = \cos \varpi_q z^* - s_m \varpi_q \sin \varpi_q z^* \quad \text{for } q = 1, 2, 3, 4 \quad (2.57)$$

$$s_m \varpi_q = \cot \varpi_q \quad \text{for } q = 1, 2, 3, 4, \quad (2.58)$$

where the vertical basis functions are nonorthogonal. Once again, a complete discussion of the vertical basis functions and eigenvalues is found in Appendix B.

Next, we substitute the temperature expansion (2.42) and, when required, the streamfunction expansions (2.55)–(2.56) into each term of the thermodynamic equation (2.25). We then multiply each term by the appropriate basis function and integrate over the domain  $0 \leq x^* \leq 1, 0 \leq y^* \leq 1, 0 \leq z^* \leq 1$ . We use the following identities to simplify the equations:

$$\int_0^1 \sin 2\pi x^* \sin 2\pi x^* dx^* = 1/2 \quad (2.59)$$

$$\int_0^1 \sin 2\pi x^* \cos 2\pi x^* dx^* = 0 \quad (2.60)$$

$$\int_0^1 \sin 2\pi m y^* \sin 2\pi n y^* dy^* = 1/2 \quad (2.61)$$

$$\int_0^1 \sin 2\pi m y^* \cos 2\pi n y^* dy^* = 0, \quad (2.62)$$

and realize that only integrals involving squares of horizontal functions are nonzero. We thus conclude for the linear terms that we only obtain nonzero integrals when  $i = k$  in the equation

$$\int_0^1 \int_0^1 \text{trig}_i(x^*, y^*) \text{trig}_k(x^*, y^*) dx^* dy^* = 1/4. \quad (2.63)$$

For the nonlinear term in the thermodynamic equation, we must consider integrals of triple products and, therefore, must establish selection rules to determine the nonzero integrals.

These rules specify that the integral

$$\int_0^1 \int_0^1 \text{trig}_i(x^*, y^*) \text{trig}_k(x^*, y^*) \text{trig}_m(x^*, y^*) dx^* dy^* = 1/4, \quad (2.64)$$

exactly when

$$i = 0 \text{ and } k = m$$

$$\text{or } k = 0 \text{ and } i = m$$

$$\text{or } m = 0 \text{ and } i = k.$$

We also observe, using the Lagrange Identity for orthogonal functions, that

$$\int_0^1 F_j(z^*) F_l(z^*) dz^* = 0, \quad j \neq l, \quad (2.65)$$

and so we can eliminate expressions containing this integral. The remaining integrations of vertical basis functions are evaluated using the DERIVE software integration routine and simplifications given by the following relationships:

$$s_T \omega_1 = \tanh \omega_1, \quad (2.66)$$

$$\sin \omega_j = \frac{-s_T \omega_j (-1)^j}{(1 + s_T^2 \omega_j^2)^{1/2}} \quad (2.67)$$

$$\cos \omega_j = \frac{-(-1)^j}{(1 + s_T^2 \omega_j^2)^{1/2}} \quad (2.68)$$

$$s_T \omega_j = \tan \omega_j, \quad (2.69)$$

for  $j = 2, 3, 4$ ,

and

$$\sin \varpi_q = \frac{-(-1)^q}{(1 + s_m^2 \varpi_q^2)^{1/2}} \quad (2.70)$$

$$\cos \varpi_q = \frac{-s_m \varpi_q (-1)^q}{(1 + s_m^2 \varpi_q^2)^{1/2}} \quad (2.71)$$

$$s_m \varpi_q = \cot \varpi_q, \quad (2.72)$$

for  $q = 1, 2, 3, 4$ . Integrations of vertical basis functions in the mean wind advection term

are of the form  $\int_0^1 V^*(z^*) F_j(z^*) F_l(z^*) dz^*$  and are evaluated using an IMSL subroutine.

We next substitute expansions (2.55)–(2.56), using the relationship given by (2.54), into each term of the vorticity equation (2.33). We once again multiply each term by the appropriate basis function and integrate over the spatial domain. We use the trigonometric integral identities (2.59)–(2.62) to eliminate all expressions except those of the form

$$\int_0^1 \int_0^1 \text{trig}_p(x^*, y^*) \text{trig}_c(x^*, y^*) dx^* dy^* = 1/4, \quad p = c. \quad (2.73)$$

For the nonlinear term, we retain expressions of the form

$$\int_0^1 \int_0^1 \text{trig}_p(x^*, y^*) \text{trig}_r(x^*, y^*) \text{trig}_c(x^*, y^*) dx^* dy^* = 1/4, \quad (2.74)$$

where

$$p = 0 \text{ and } r = c$$

or  $r = 0$  and  $p = c$

or  $c = 0$  and  $p = r$ .

Owing to the nonorthogonality of the momentum vertical basis functions, we cannot eliminate any expressions based on integrals of these functions. The integrals are evaluated using the DERIVE software integration routine and the relationships (2.66)-

(2.72). The mean wind advection term integrals of the form  $\int_0^1 V^*(z^*) h_q(z^*) h_d(z^*) dz^*$  are also evaluated using an IMSL subroutine; integrals involving  $\partial V / \partial z^*$  can be put in the above form via integration by parts (e.g. Shirer 1986).

### 2.3. The Computer Model

The computer code used to represent the physical and mathematical model presented in the previous sections is written in the FORTRAN programming language. It is compiled using the WATFOR77 compiler. The first part of the code determines the values for  $\omega_j$  for  $j = 1, 2, 3, 4$ , and  $\varpi_q$  for  $q = 1, 2, 3, 4$ , based on input values for the constants  $s_m$  and  $s_T$ . The values of these constants are provided by the subroutine discussed in Appendix A. An iterative technique is used to solve (2.50)-(2.51), (2.53), and (2.58) for the eigenvalues. Prior to integrating the system, we must also input values for the parameters  $l, m, a_x, a_y, \beta, \mu, Ra, Re$ , and  $P$ .

The determined and input values are used to fill the  $60 \times 60$  matrices representing the terms in the spectral system. The individual matrices that compose  $A$ ,  $B$ , and  $C$  are grouped as temporal derivative term matrices, linear term matrices, and nonlinear term

matrices. We can rewrite (2.25) and (2.33) in terms of this matrix notation:

$$A_1 \dot{y} = B_1 y + C_1(y)y \quad (2.75)$$

$$A_2 \dot{y} = B_2 y + C_2(y)y. \quad (2.76)$$

All the matrices in a given group are then added together:

$$A = A_1 + A_2 \quad (2.77)$$

$$B = B_1 + B_2 \quad (2.78)$$

$$C(y) = C_1(y) + C_2(y). \quad (2.79)$$

This gives the system (2.40)-(2.41). The temporal derivative term matrix and the linear term matrix are filled prior to the integration because  $A$  and  $B$  do not depend on the spectral coefficient in  $y$ . An IMSL routine computes  $A^{-1}$  and a different IMSL routine computes  $A^{-1}B$ . The nonlinear term matrix must be filled before each integration time step because  $C$  depends on  $y$ . The calculation  $A^{-1}C(y)$  must also be done before each time step.

The IMSL integration routine uses the Adams-Gear method and requires user-supplied initial conditions for the 60-element vector  $y$ . At each time step, an IMSL routine calculates  $A^{-1}By$  and  $A^{-1}C(y)y$ . The two resulting 60-element vectors are added together to give the right sides of the 60 equations for which we are solving. The integration routine uses these results to calculate new values for the 60 time-dependent amplitude coefficients after each time step. We integrate the model until the square root of the sum of the squares of the coefficients equilibrates. After the model integration is

complete, these amplitude coefficients are used to construct the model solution using (2.4) and (2.55)-(2.56). Examples of this solution are given in the following chapter.

## Chapter 3

### MODEL EVALUATION

In order to investigate whether the model solutions represent the expected physical processes, we performed a series of model integrations and analyses. The integrations included varying the physical parameter values, changing the initial conditions, or using various numerical integration techniques. The analyses included various eigensystem evaluations and graphical representations of the evolution of the solution. These various procedures were used not only to test the validity of the physical assumptions made, but also to identify and correct any computer programming errors. The results of these integrations and analyses are presented in Section 3.1.

Once we chose the physical parameter values, we performed a simple case study to evaluate the quality of the model solutions. This study allows us to examine the patterns produced by the roll circulations and the associated vertical transfers of heat and momentum. By comparing these results with those of other models, we can assess the performance of our model and the effects of incorporating the forcing rates in the lower vertical boundary conditions. The results of this case study are given in Section 3.2.

#### 3.1. Parameter Values and Initial Conditions

The first physical parameter values to be determined are those given by the basic states of the atmosphere and sea surface. These parameter values are input into the subroutine described in Appendix A that determines values for the surface roughness,  $z_0$ , and the Monin-Obhukov length,  $L$ . The values obtained for  $z_0$  and  $L$  are then used in another subroutine that calculates values for the two constant lower boundary forcing

parameters,  $s_m$  and  $s_T$ . The parameter values used in the model case study are given in

Table 3.1.

Table 3.1. Parameter values used in the model.

PARAMETER	VALUE
ASPECT RATIO IN THE X-DIRECTION ( $a_x$ )	0.001
ASPECT RATIO IN THE Y-DIRECTION ( $a_y$ )	0.7
HEIGHT OF TOP OF DOMAIN ( $Z_T$ )	1000 m
HEIGHT OF BOTTOM OF DOMAIN ( $h_{LB}$ )	10 m
U MEAN WIND SPEED AT $Z = Z_T$	$2.5 \text{ ms}^{-1}$
U MEAN WIND SPEED AT $Z = h_{LB}$	$2.5 \text{ ms}^{-1}$
V MEAN WIND SPEED AT $Z = Z_T$	$2.5 \text{ ms}^{-1}$
V MEAN WIND SPEED AT $Z = h_{LB}$	$2.5 \text{ ms}^{-1}$
GRAVITY ( $g$ )	$9.8 \text{ ms}^{-2}$
CORIOLIS PARAMETER ( $f$ )	$0.0 \text{ s}^{-1}$
EDDY VISCOSITY ( $\nu$ )	$10 \text{ m}^2\text{s}^{-1}$
EDDY CONDUCTIVITY ( $\kappa$ )	$10 \text{ m}^2\text{s}^{-1}$
PRANDTL NUMBER ( $P$ )	1.0
SEA SURFACE TEMPERATURE ( $T_\infty$ )	293 K
TEMPERATURE AT $Z = h_{LB}$	$5^\circ \text{ C}$
MIXING RATIO AT SEA SURFACE	$6.0 \text{ g kg}^{-1}$
MIXING RATIO AT $Z = h_{LB}$	$1.5 \text{ g kg}^{-1}$
RAYLEIGH NUMBER ( $Ra$ )	$2.75 \times 10^5$
REYNOLDS NUMBER ( $Re$ )	350

In an effort to keep the system simple for the case study, we use a constant wind speed of  $2.5 \text{ ms}^{-1}$  in both the  $x$ - and  $y$ -directions. This gives a total wind vector of magnitude  $3.54 \text{ ms}^{-1}$ . We choose aspect ratios of 0.001 in the  $x$ -direction and 0.7 in the  $y$ -direction to produce a quasi-two-dimensional domain oriented approximately in the  $y$ - $z$  plane. The most important parameter values supplied to the initial subroutine are those for the sea surface temperature and the 10  $m$  temperature. The surface layer vertical temperature difference  $\Delta T$  calculated from these two parameters determines the amount of thermal energy being supplied to the system through the lower boundary. This  $\Delta T$  differs from  $\Delta_s T$ , which is the basic state temperature difference between heights  $z_r$  and  $h_{LB}$ . In Table 3.2 we present various values of  $\Delta T$  for fixed values of the other parameters, together with the associated values of  $z_o$ ,  $L$ ,  $s_m$ , and  $s_T$ .

Table 3.2. Parameter values for surface layer  $\Delta T$  and associated calculated values for  $z_o$ ,  $L$ ,  $s_m$ , and  $s_T$ .

$\Delta T(^{\circ}\text{C})$	$z_o(m)$	$L(m)$	$s_m$	$s_T$
1°	$0.27425 \times 10^{-4}$	-4.6468	0.277716	0.491370
5°	$0.27533 \times 10^{-4}$	-1.9084	0.328111	0.704164
10°	$0.27733 \times 10^{-4}$	-1.1104	0.361833	0.875182
15°	$0.27936 \times 10^{-4}$	-0.78392	0.384626	1.004940
20°	$0.28134 \times 10^{-4}$	-0.60487	0.402118	1.112800

For our case study, we choose the relatively strong forcing value of  $\Delta T = 15^{\circ}\text{C}$  and use the associated values shown in Table 3.2 for  $s_m$  and  $s_T$ . We note that  $s_T > 1$  here so that the first temperature eigenfunction is given by (2.49) and (2.51). Smaller values for  $\Delta T$

would require us to use the hyperbolic first temperature eigenfunction given by (2.48) and (2.50). This hyperbolic case remains untested.

Once we have determined the values for  $s_m$  and  $s_T$ , the computer program, using relationships (2.51), (2.53), and (2.58), calculates the eigenvalues  $\omega_j$  and  $\varpi_q$  for  $j = q = 1, 2, 3, 4$ . These values for the case study are given in Table 3.3. We can use these values and the vertical basis functions (2.49), (2.52), and (2.57) to plot profiles for temperature and vertical velocity. These plots are given in Figs. 3.1-3.2. They indicate that temperature and vertical velocity are well correlated. The temperature profile reveals that the eigenfunction for wavenumber 1 gives a linear relationship, as seen in observations, that is consistent with the basic state, and succeeding eigenfunctions superimpose trigonometric functions on this linear relationship. The maximum in temperature at the lower boundary is consistent with the thermal forcing occurring there. The vertical velocity profile is similar, and although largest at  $z^* = 0$ , a maximum in vertical velocity conceivably could occur above the lower boundary through interaction of the different eigenfunctions.

Table 3.3. Case study values for  $\omega_j$  and  $\varpi_q$  for  $j = q = 1, 2, 3, 4$ .

	$\omega_j$	$\varpi_q$
$j = q = 1$	0.121378	1.153289
$j = q = 2$	4.494503	3.748059
$j = q = 3$	7.725888	6.655595
$j = q = 4$	10.904572	9.686992

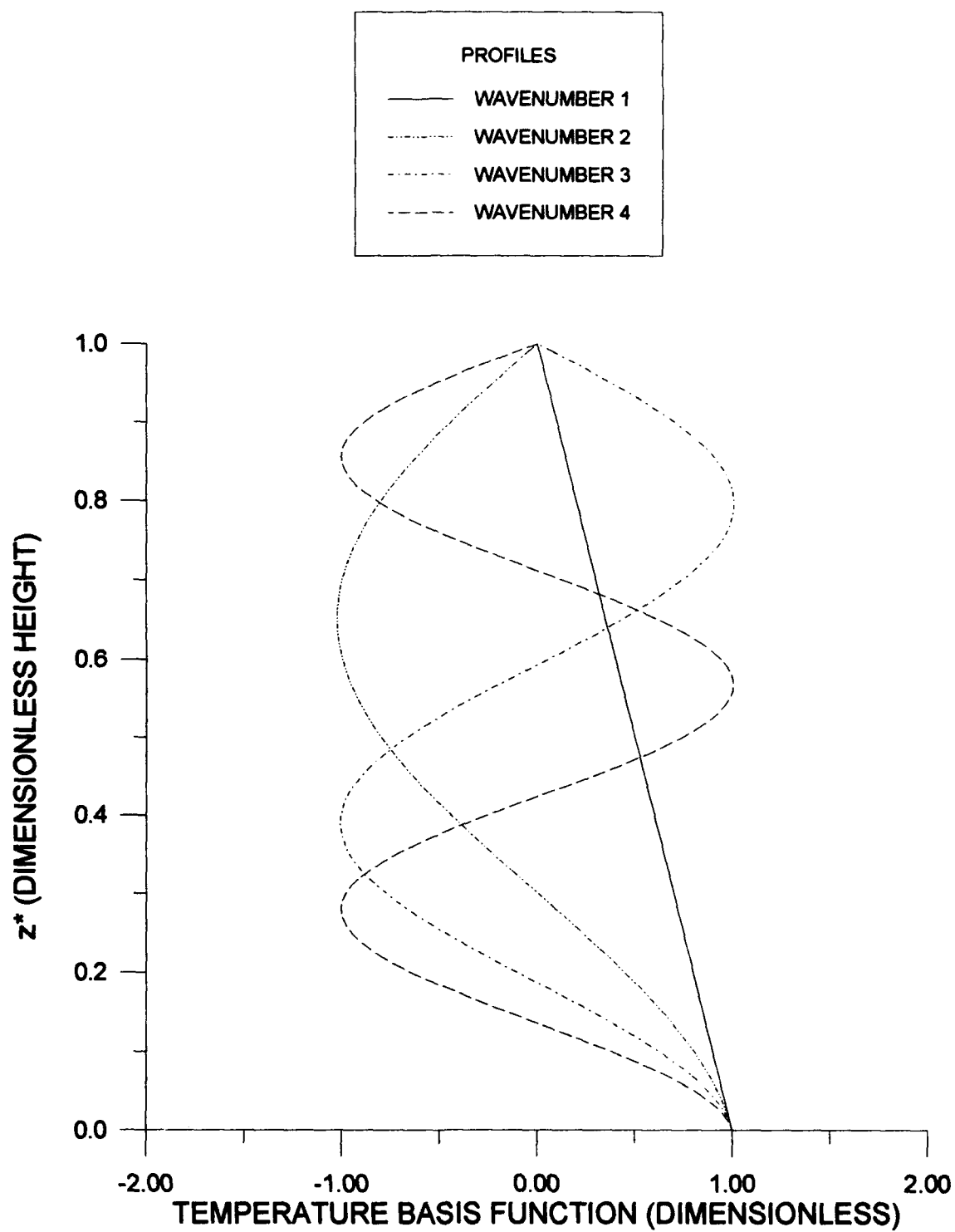


Fig. 3.1. Temperature vertical basis function profiles for the four wavenumbers chosen.

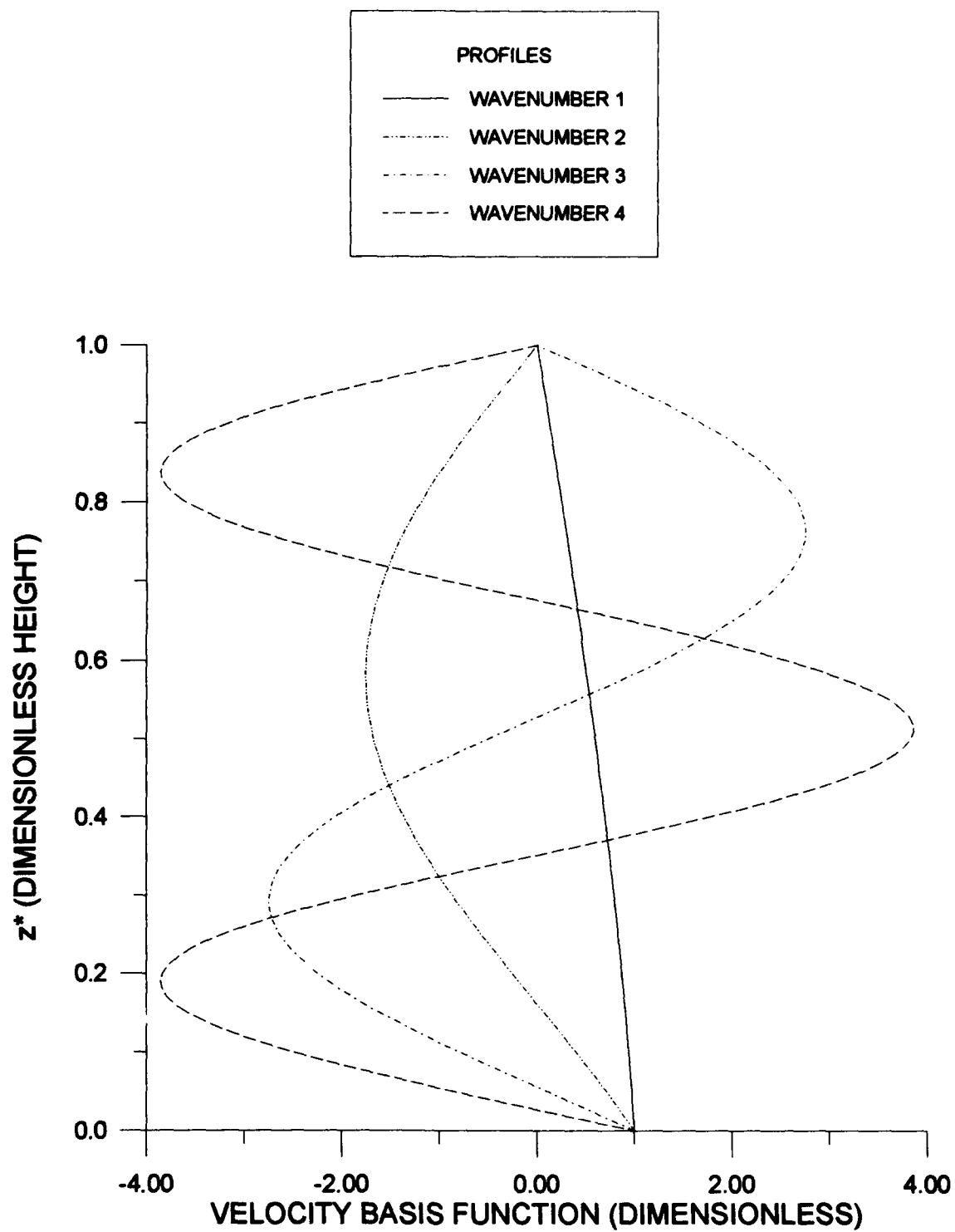


Fig. 3.2. Velocity vertical basis function (vertical velocity) profiles for the four wavenumbers chosen.

The initial conditions represented by the initial values of the 60 time-dependent amplitude coefficients are determined using an eigensystem analysis. We find the eigenvectors associated with the conjugate pair of eigenvalues whose real parts change sign with a change in the forcing rate. Thus these eigenvectors tell us the relative magnitudes of the coefficients that would approximate their values in the nonlinear branching solution. We can multiply these eigenvectors by a constant to obtain values on the scale of the model amplitude coefficients using the dimensionless conversions, and so the resulting values as initial conditions.

As noted in Chapter 2, the IMSL integration routine uses the Adams-Gear method. A series of model integrations were performed to determine the proper value for the time step. The time step was reduced until the number of internal subroutine calls was small enough to allow accurate solutions at each step. We determined the largest possible time step to be 0.1 seconds, which corresponds to the dimensionless time value of  $1.02 \times 10^{-6}$ . Model integrations were run for 5 hours, which corresponds to 180,000 time steps, to allow sufficient time for the system to equilibrate.

Because we expect the roll solutions to have time scales on the order of an hour or less, we neglect the Coriolis term in the model. We specify only one wavenumber in the  $x$ - and  $y$ -directions, and so we set  $l = 1$  and  $m = 1$ . The values chosen for  $\nu$  and  $\kappa$  determine the value of the Prandtl number  $P$  using (2.30). In this case,  $\nu = \kappa = 10 \text{ m}^2 \text{ s}^{-1}$ , which gives  $P = 1$ . We also choose  $\beta = \mu = 1$  for the numerical dissipation terms. The value for the dimensionless Reynolds number  $Re$  is found using (2.28) based on a value of the wind speed ( $3.54 \text{ m s}^{-1}$ ) at the top of the domain and a domain height of  $1000 \text{ m}$ ; the result is  $Re = 350$ . The value used for the dimensionless parameter  $Ra$  is determined based on a stability analysis.

Ideally, we would choose a value for  $Ra$  that produces a conjugate pair of eigenvalues having slightly positive real parts in the linear stability analysis. This result signals a Hopf bifurcation producing a periodic solution that, if supercritical and hence stable, is realized after the system transients have disappeared (e.g. Pyle 1987). Unfortunately, during the integrations performed for this study, the bifurcating model solutions did not equilibrate, indicating a source of energy that is not currently being damped properly. This problem will be discussed further in Chapter 4. We therefore choose a case for which all the real parts of the eigenvalues are negative and so the solution is damping. By finding a value for  $Ra$  that produces a very slowly damping solution, we can simulate a system approaching an attractor. We choose  $Ra = 2.75 \times 10^5$  that corresponds to  $\Delta_s T = 0.85^\circ\text{C}$  across the domain. This allows us to integrate the model without obtaining excessive growth or decay on time scales appropriate for boundary layer rolls.

By plotting the square root of the sum of the squares of the 60 time-dependent amplitude coefficients, we can determine when the system has reached a quasi-equilibrated state. A plot of the square root of the sum of the squares is given in Fig. 3.3. This plot indicates that it takes approximately 5 hours for the major transients to disappear using the initial conditions determined from the eigenvectors. We have considered the possibility of a subcritically branching bifurcating solution; but integrating the system further reveals that the solution continues to damp very slowly, indicating that such a subcritical solution is not likely.

We can also check the validity of the model by examining the periodicity of the solution. Using a linear eigensystem analysis, we can determine the values for the imaginary parts  $\text{Im}$  of the eigenvalues. The limiting period of the bifurcating solution is

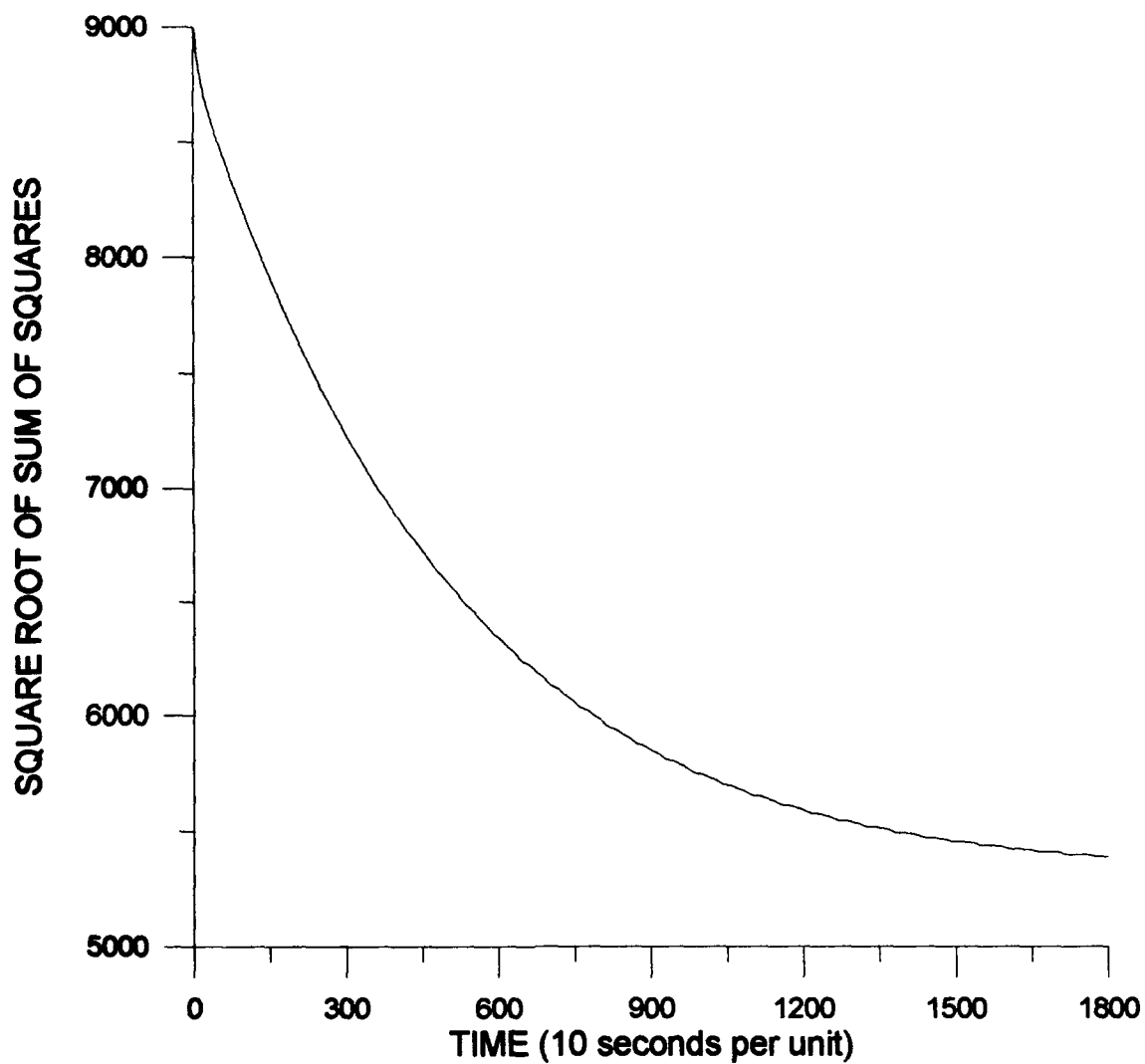


Fig. 3.3. The square root of the sum of the squares for the 60 time-dependent amplitude coefficients, demonstrating that the system is approaching a state of quasi-equilibration.

determined by calculating (Pyle 1987)

$$Period = \frac{2\pi}{Im} \quad (3.1)$$

This value must then be converted to dimensional units using (2.19). Based on our analysis,  $Im = 1086$ . Using (3.1), we find a dimensionless period of  $5.786 \times 10^{-3}$ , or 9.45 minutes.

Given our constant wind profile, this period should correspond to the speed of movement of the rolls caused by advection by the mean wind. To find this speed, we first note that the ratio  $L_y/L_x = a_x/a_y$  serves as a measure of the orientation angle  $\theta$  of a roll-type solution, for which  $\tan \theta = a_x/a_y$ ; here  $\theta$  is the angle between the roll axis and east. At any level, the background wind angle  $\phi$  is given by  $\tan \phi = V/U = V^*/U^*$ . Thus it follows that the angle  $\phi - \theta$  between the background wind vector and the roll axis obeys

$$\tan(\phi - \theta) = \frac{\tan \phi - \tan \theta}{1 + \tan \phi \tan \theta} = \frac{a_y V^* - a_x U^*}{a_y U^* + a_x V^*} \quad (3.2)$$

For the case discussed here,  $a_x = 0.001$  and  $a_y = 0.7$ , the rolls are aligned nearly along the  $x$ -axis, and so, with the constant values  $U = V = 2.5 \text{ ms}^{-1}$ , the angle  $\phi - \theta$  between the mean wind direction and the roll is approximately  $45^\circ$ . This result is also given by (3.2) in which  $\tan(\phi - \theta) \approx 1$  for  $a_x \ll a_y$  and  $U^* = V^*$ . This means that advection is accomplished predominantly by the  $V$  component, as expected from (2.25)-(2.26) when  $a_x \ll a_y$ .

From the above argument, we find that the mean cross-roll wind is given approximately by  $V = 2.5 \text{ ms}^{-1}$ . The distance between the rolls is approximately 1400 m,

which produces a period of 9.33 minutes that is close to the value of 9.45 minutes given by (3.1). We next check these values for the period against the nonlinear results for two of the time-dependent amplitude coefficients given by the numerical integration. The period given by each graph in Figs. 3.4-3.5 is approximately 9.3 minutes, therefore demonstrating that the model integration is accurately reproducing the expected periodicity of the solution.

### 3.2. Case Study

We use the physical parameter values determined in Section 3.1 to examine a single case of forced boundary layer roll circulations. Our goal is to determine whether the model correctly captures the patterns produced by the rolls and to verify the behavior of the various physical quantities. Because we have chosen a case in which the solution is damping, the magnitudes of the physical quantities are not necessarily representative of the actual physical solution. However, the planview patterns and profiles produced can be analyzed using the dimensionless quantities given by the model.

Our first step is to determine whether the model captures the proper spatial organization of the roll circulations. One way of examining this structure is to analyze the vertical velocity field at the lower boundary. In Fig. 3.6 we present such an analysis in the dimensionless  $x^*-y^*$ -plane at  $z^* = 0$ . This corresponds to the height  $h_{LB}$  of the lower boundary, which is 10 *m* above the sea surface. The areas of light shading indicate positive vertical velocities and the areas of dark shading indicate negative vertical velocities. There are distinct bands of positive and negative vertical velocities that suggest the model is capturing the spatial organization of the roll circulations. As expected, there is no net vertical motion across any horizontal plane.

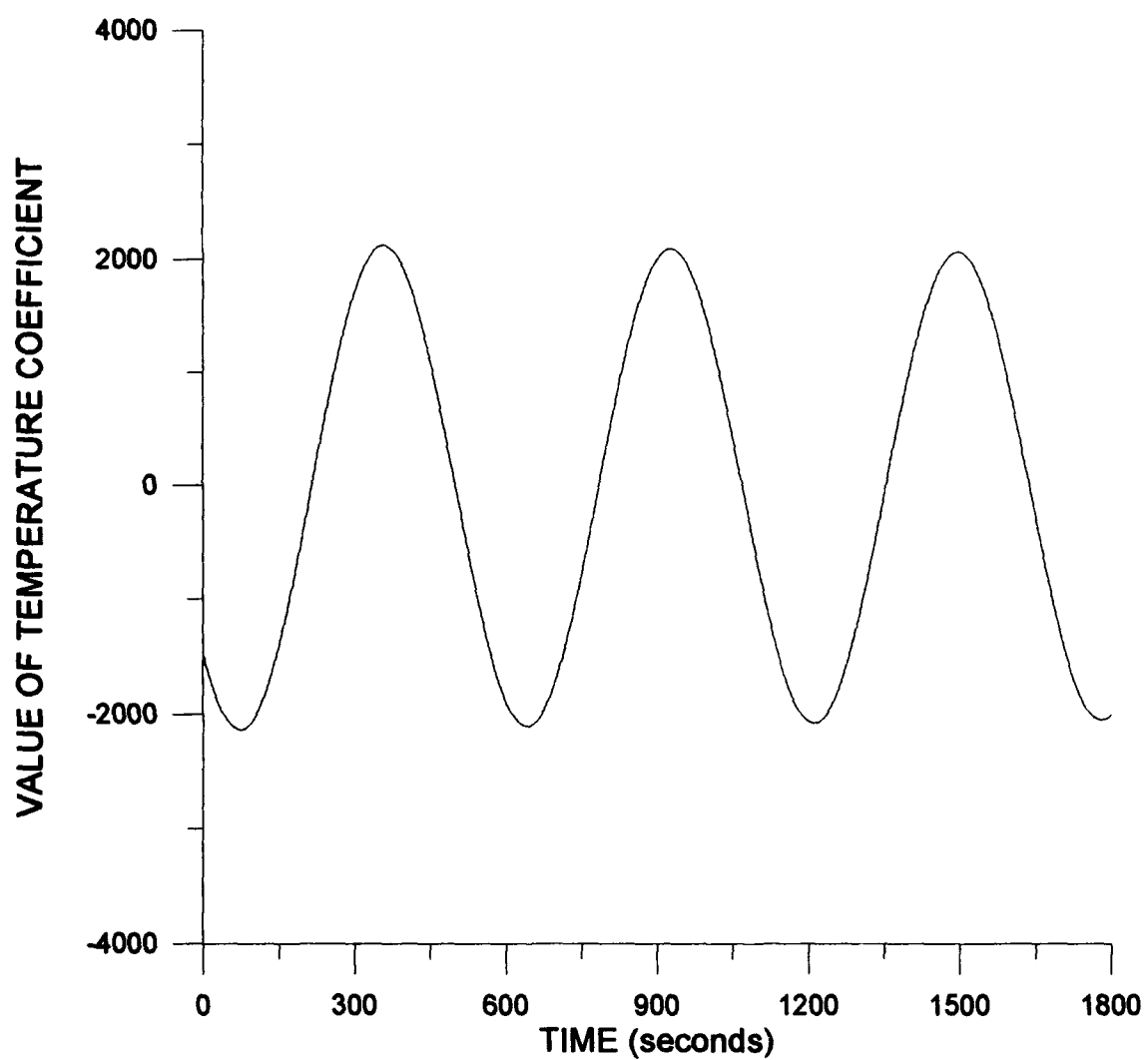


Fig. 3.4. Time series of one of the time-dependent temperature amplitude coefficients ( $T_{11}$ ), demonstrating that the bifurcating solution has a period of approximately 9.3 minutes.

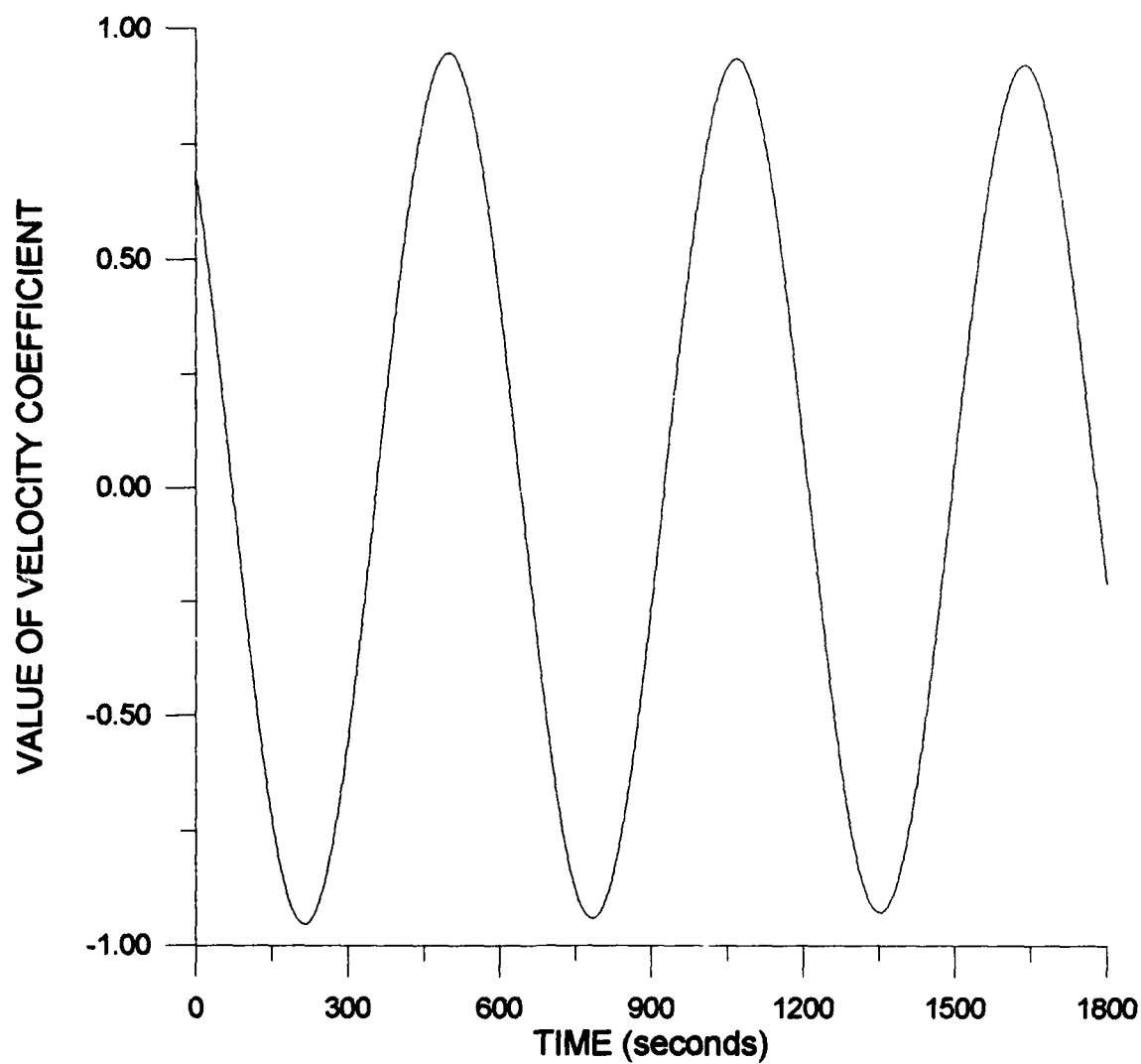


Fig. 3.5. Time series of one of the time-dependent velocity amplitude coefficients ( $\psi_{11}$ ), demonstrating that the bifurcating solution has a period of approximately 9.3 minutes.

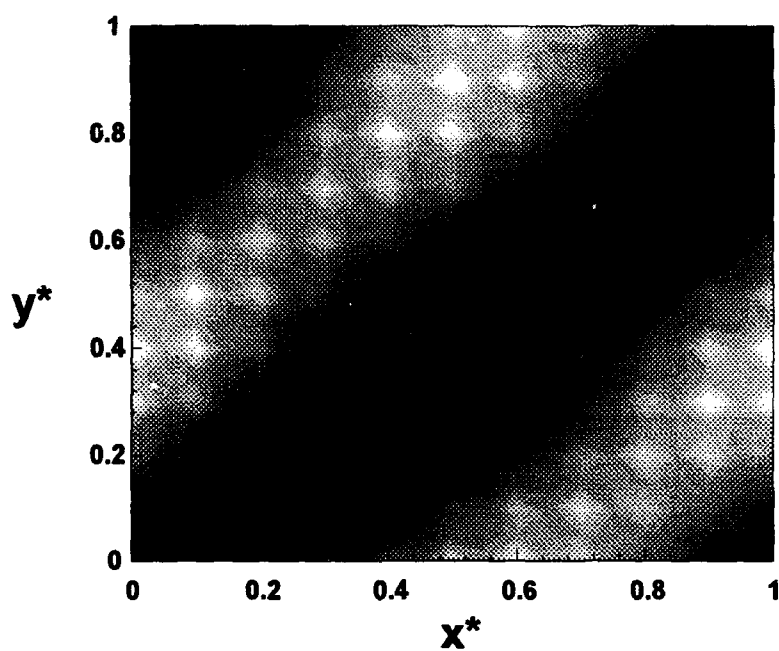


Fig. 3.6. Planview of vertical velocity  $w^*$  in the dimensionless coordinate system at the height  $h_{LB}$  of the lower boundary. Areas of light shading indicate positive vertical velocity and areas of dark shading indicate negative vertical velocity. The cellular pattern parallel to the roll is an artifact of the graphics routine.

As a consequence of the aspect ratios we have chosen, the roll pattern actually aligns itself a bit differently in the dimensional coordinate system. The aspect ratio in the  $x$ -direction,  $\alpha_x = 0.001$ , corresponds to a roll wavelength component of  $990 \text{ km}$  and the aspect ratio in the  $y$ -direction,  $\alpha_y = 0.7$ , corresponds to a roll wavelength component of  $1.414 \text{ km}$ . This observation means that in dimensional space, the rolls would actually align themselves almost parallel to the  $x$ -axis, with spacing between the rolls on the order of  $1.4 \text{ km}$ . This two-dimensional planform is consistent with observations of roll patterns, although the orientation of  $45^\circ$  to the right of the mean wind is not. For this case study, we choose such a large orientation angle to yield a periodic solution dominated by the advective period.

Another way of examining the roll structure and of ensuring that the rolls are actually transferring heat from the sea surface into the boundary layer is to analyze the spatial pattern of the heat flux at the lower boundary. We would expect areas of positive heat flux to be correlated with the areas of positive vertical velocity. In Fig. 3.7 we present this vertical heat flux analysis. The areas of light shading indicate positive heat flux and the areas of dark shading indicate negative heat flux. As can be seen, the areas of positive and negative heat flux are well correlated with the areas of positive and negative vertical velocity in Fig. 3.6.

We next analyze the vertical heat flux  $w^*T^*$  profile integrated over the  $x^*-y^*$ -plane. The profile, given in Fig. 3.8, indicates a net positive heat flux over the entire domain that is consistent with a net transfer of heat from the sea surface into the boundary layer. We would expect this heat flux to be largest close to the sea surface and to decrease linearly with height as indicated by observations (Lilly 1966; Stull 1988). The profile in Fig. 3.8 is consistent with this linear decrease with height and only changes slope to accommodate the upper boundary condition we imposed on the system. The modification of

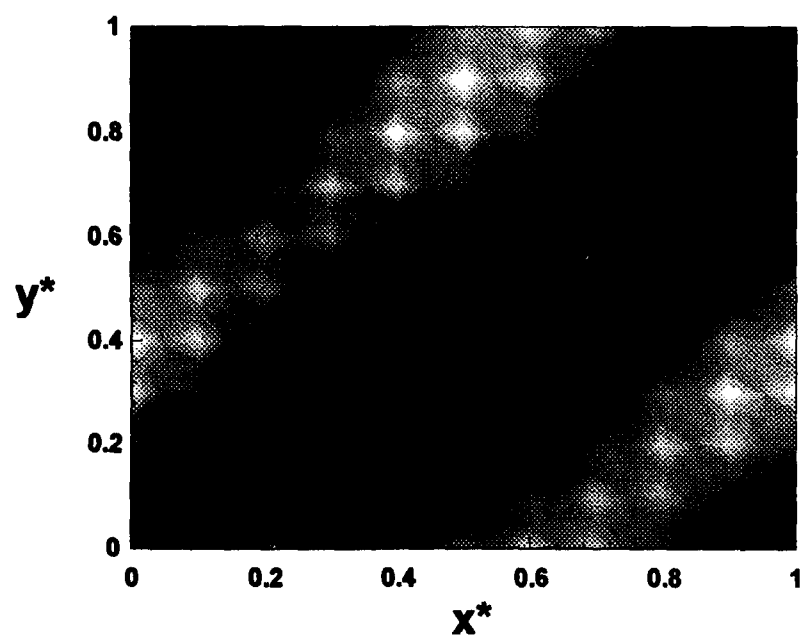


Fig. 3.7. Planview of vertical heat flux  $w'T'$  in the dimensionless coordinate system at the height  $h_{\text{LB}}$  of the lower boundary. Areas of light shading indicate positive heat flux and areas of dark shading indicate negative heat flux. The cellular pattern parallel to the roll is an artifact of the graphics routine.

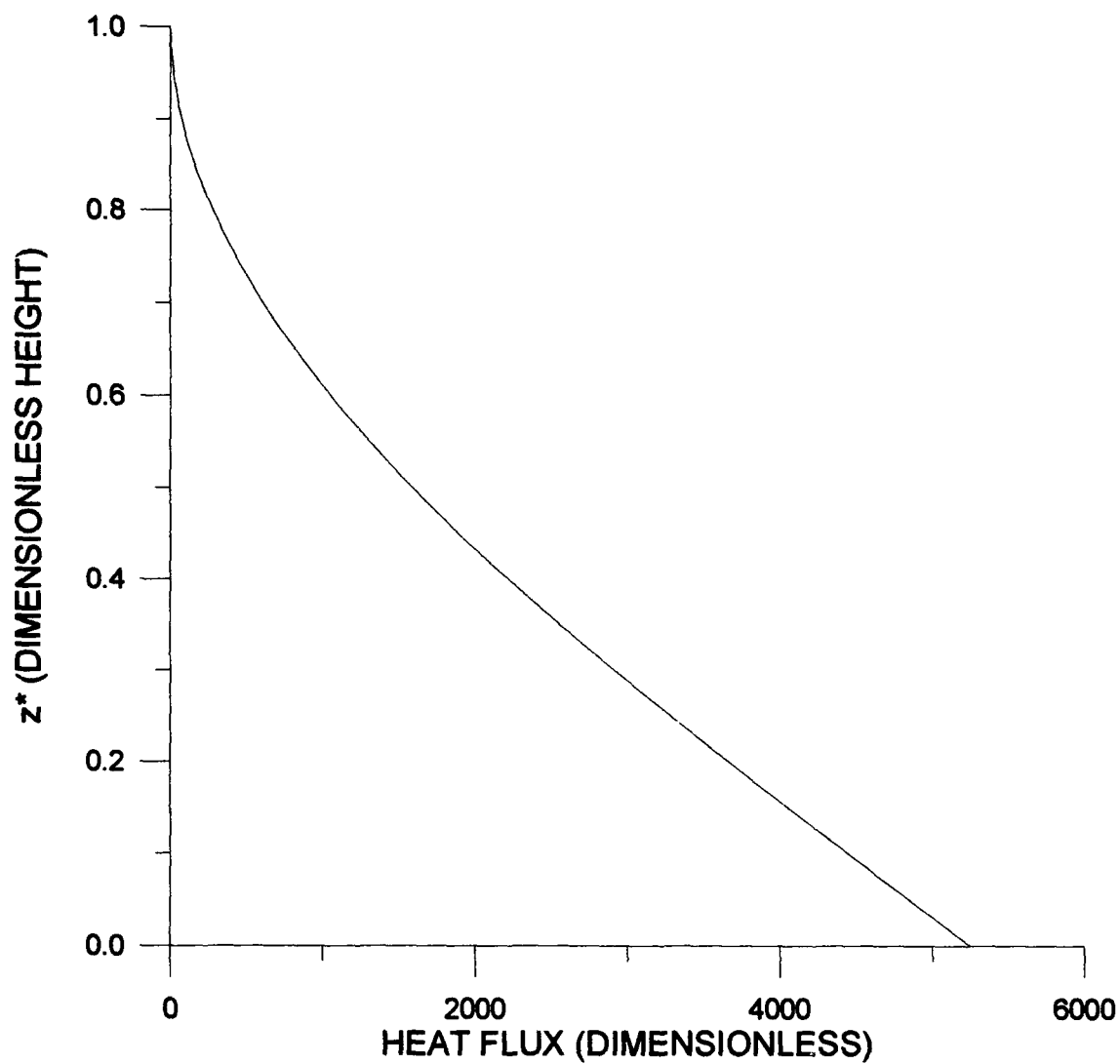


Fig. 3.8. Vertical heat flux  $w'T^*$  profile integrated over the dimensionless horizontal plane.

temperature profile by the roll circulations is given in Fig. 3.9. We construct this profile using temperature amplitude coefficients  $T_{01}$ ,  $T_{02}$ ,  $T_{03}$ , and  $T_{04}$  only, since the other contributions would integrate to zero on any plane. The profile suggests that the strong positive heat flux at the lower boundary, dominated by wavenumber 1, does indeed change the background temperature profile  $T_b(z)$  the most there, and that this change decreases linearly with height.

The fact that the circulation produces a linear profile means that the observed  $\Delta_z T$  values alone cannot be used to estimate the correct value of the Rayleigh number  $Ra$  for a model. Ideally, we would set  $Ra = 0$  in the model and compute using (2.29) the implied  $Ra$  given by  $\Delta_z T$  in Fig. 3.9. In our case, the effective  $Ra$  is the sum of the one imposed by us ( $2.75 \times 10^5$ ) and the one implied by Fig. 3.9 ( $4.50 \times 10^3$ ). Here, the value of  $Ra$  based on observed profiles would incorporate the effects of both, with each one reinforcing the other.

The two components of the vertical momentum flux profiles, given in Figs. 3.10-3.11, are found by integrating  $u^* w^*$  or  $v^* w^*$  over the  $x^*-y^*$ -plane. The profile given by the product  $u^* w^*$ , in Fig. 3.10, indicates a maximum in the transfer of negative momentum at a height of  $z^* = 0.25$ , which corresponds to 250 m in the dimensional system. This suggests that, over the domain, there is a net downward transfer of westerly wind  $u^*$  to the lower boundary from within the boundary layer. The resulting profile for  $u^*$ , given in Fig. 3.12, shows that, as suggested, momentum has been transferred downward giving larger negative  $u^*$  values at the top of the domain. This would indicate that the circulations should tilt with height.

The profile of the product  $v^* w^*$ , given in Fig. 3.11, indicates a maximum in the transfer of positive momentum at 150 m. This suggests that over the domain there is a net upward transfer of southerly wind  $v^*$  from the lower boundary into the boundary layer.

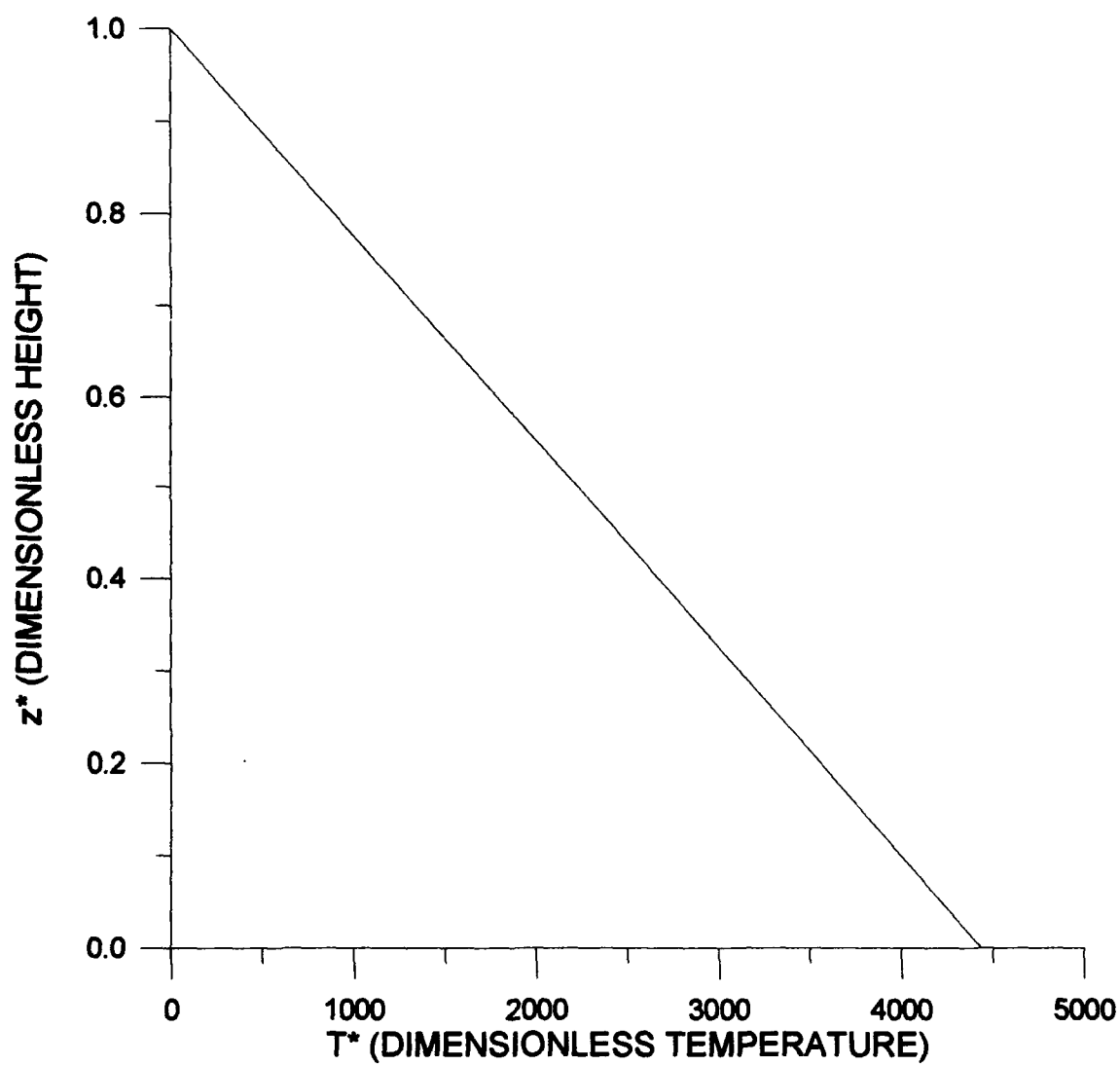


Fig. 3.9. Modification of the vertical temperature profile by the rolls.

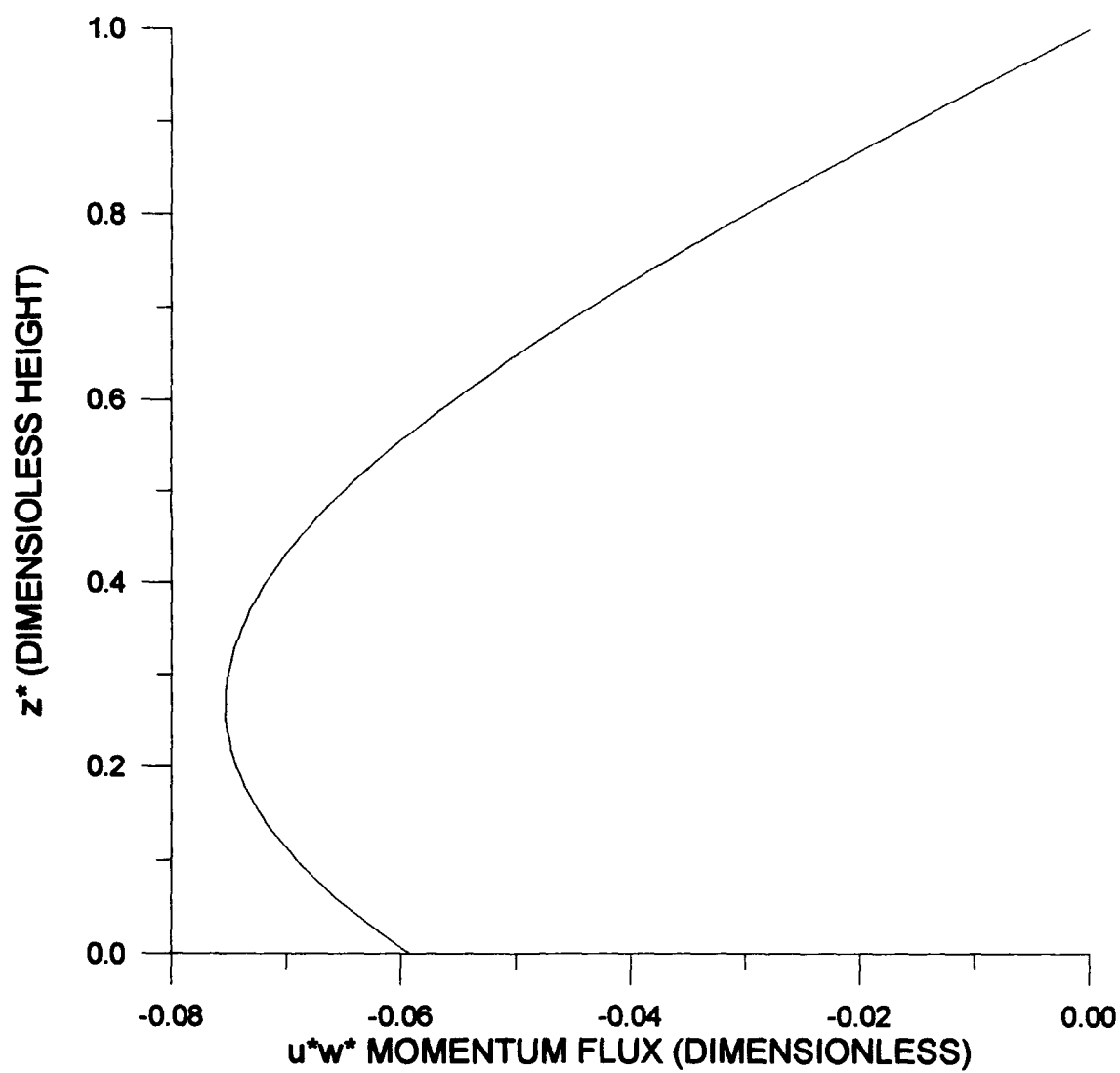


Fig. 3.10. Profile of vertical flux of westerly momentum given by integration of  $u^*w^*$  over the dimensionless horizontal plane.

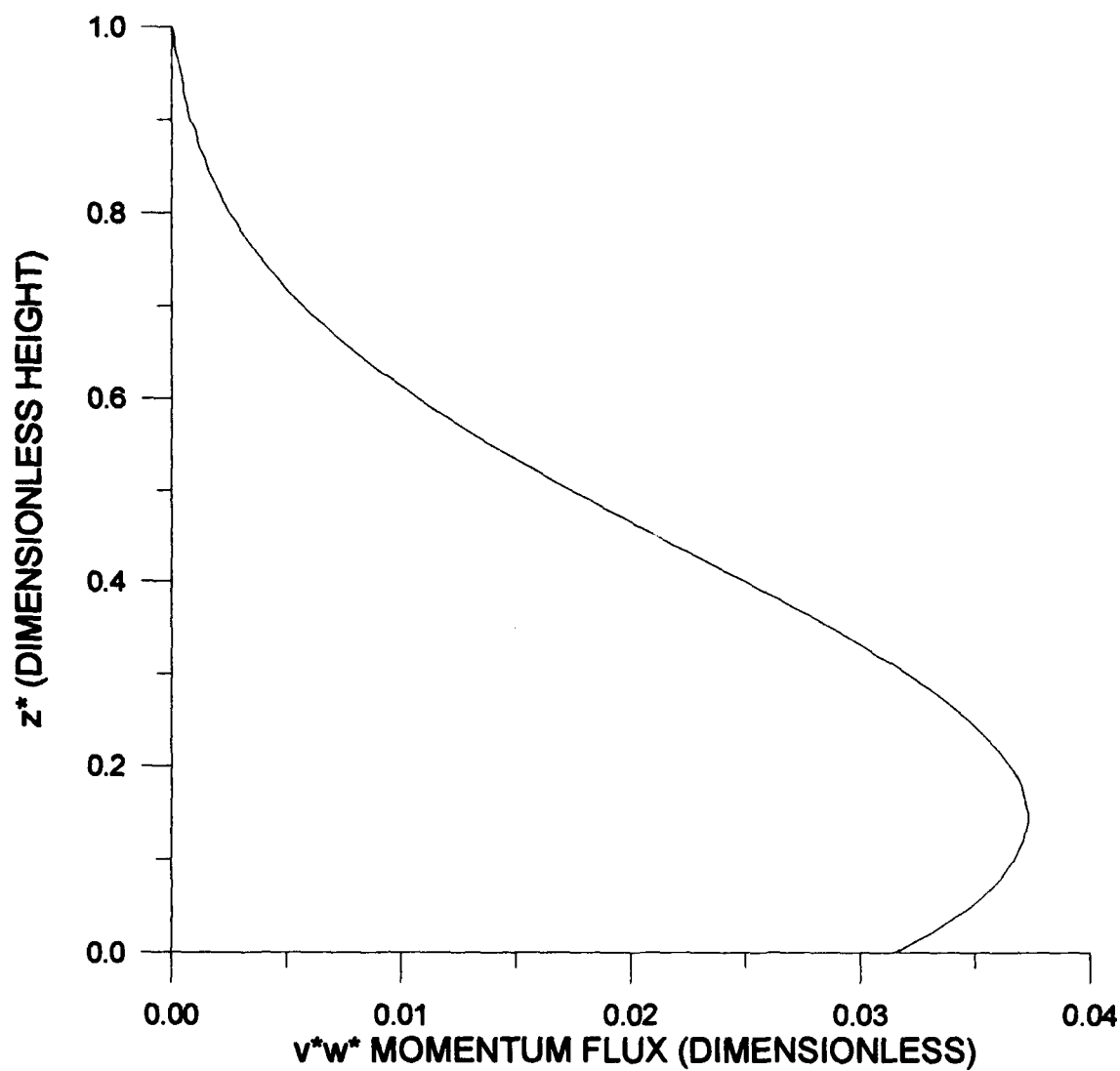


Fig. 3.11. Profile of vertical flux of southerly momentum given by integration of  $v^*w^*$  over the dimensionless horizontal plane.

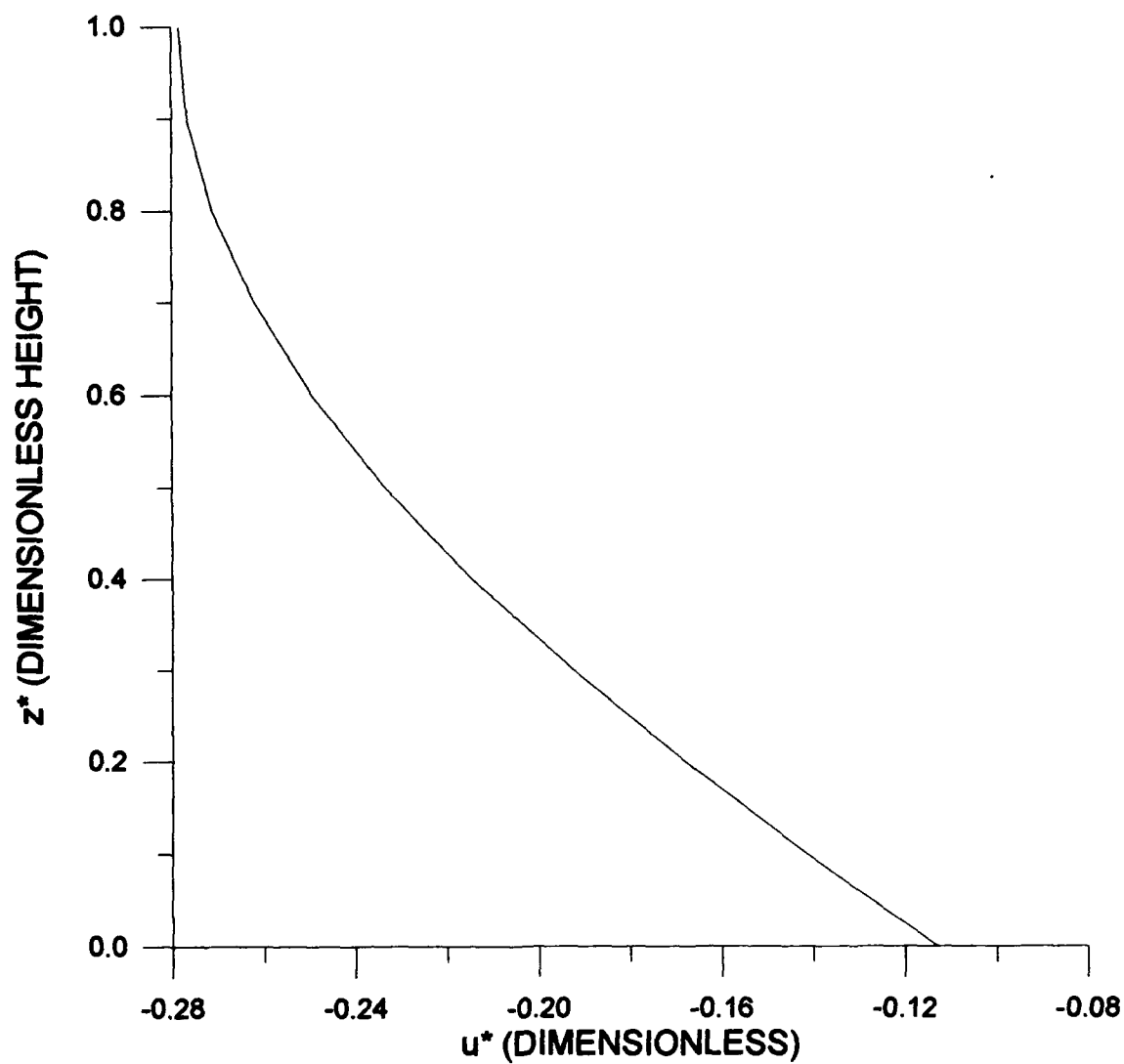


Fig. 3.12. Vertical profile for the perturbation velocity component  $u^*$  found by integrating as in Fig. 3.10. This figure also represents a modification of the basic wind profile.

The resulting profile for  $v^*$ , given in Fig. 3.13, shows that positive momentum is transferred upward giving larger positive  $v^*$  values at the top of the domain. The shapes of the vertical momentum flux profiles and associated velocity component profiles are in agreement with the results found by Brümmer and Busack (1990).

The momentum transfers indicated by our results imply that the initial constant wind profile is altered to give a southwest wind at the bottom of the domain and a more southerly wind at the top of the domain. Observations would reflect the sum of the original wind and the modified wind, meaning that an observed wind turning with height might originate from rolls formed in an environment with no wind shear. These effects, together with the fact that wind modification is predominantly linear, must be accounted for when using observed wind profiles as model input (Haack and Shirer 1992).

We next examine the vertical velocity profile for the center of an updraft given in Fig. 3.14. This graph indicates that in the updraft, the maximum vertical velocity occurs at the lower boundary and decreases to zero at the top of the domain. This result is not consistent with what is observed in the atmospheric boundary layer. We would expect from observations and other model simulations (e.g. Schmidt and Schumann 1989) that the maximum vertical velocity for an updraft would occur in the middle of the boundary layer and not at the lower boundary (see also Figs. 2.1-2.2).

Therefore, we cannot analyze the sea-surface stress patterns given by  $u^*w^*$  and  $v^*w^*$  since the vertical velocity profiles are not correct. We must determine why this inconsistency exists and correct it if we are to derive useful information about sea surface stress from this model. In the next chapter we discuss some possible solutions to explore.

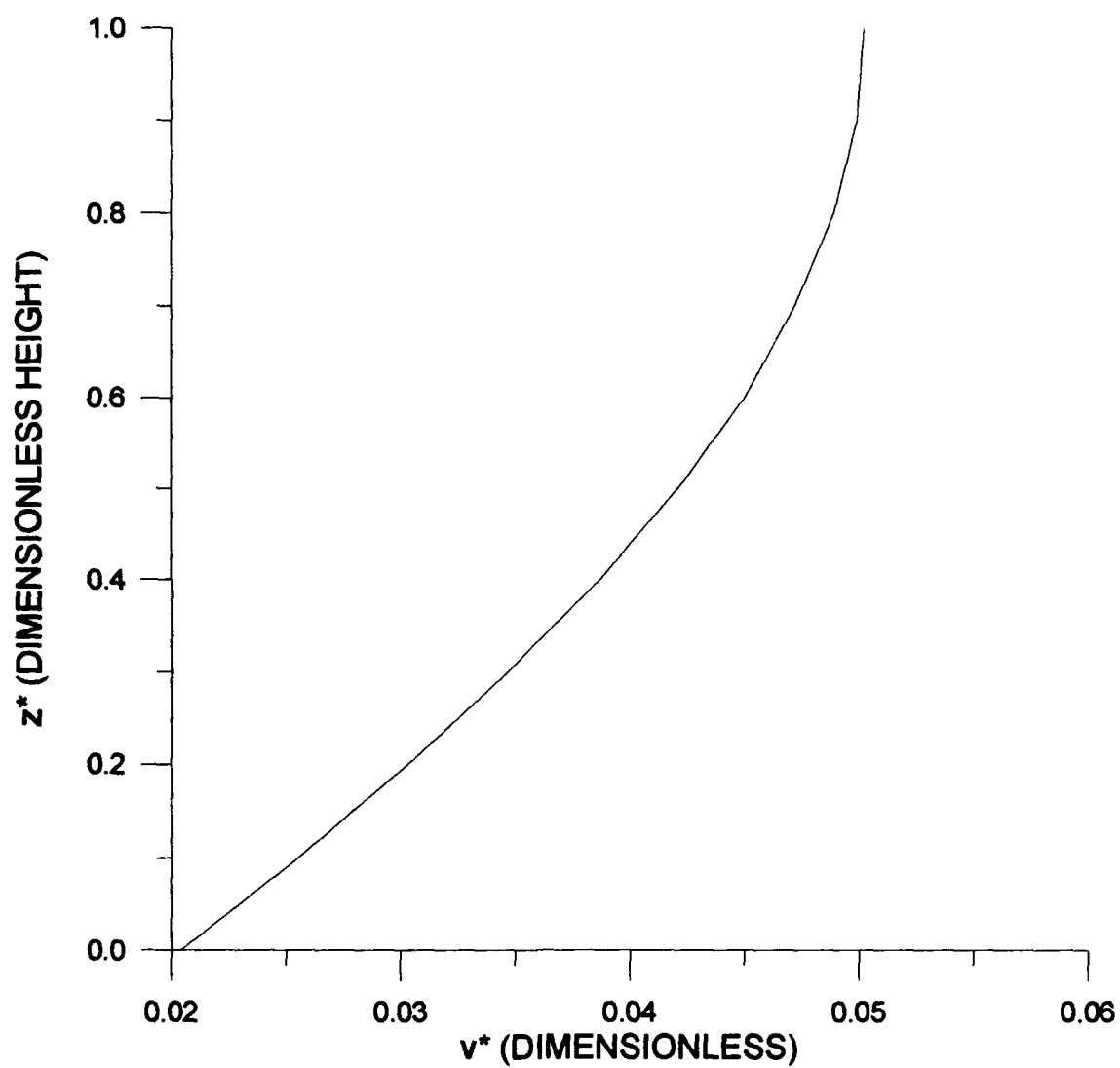


Fig. 3.13. Vertical profile for the perturbation velocity component  $v^*$  found by integrating as in Fig. 3.10. This figure also represents a modification of the basic wind profile.

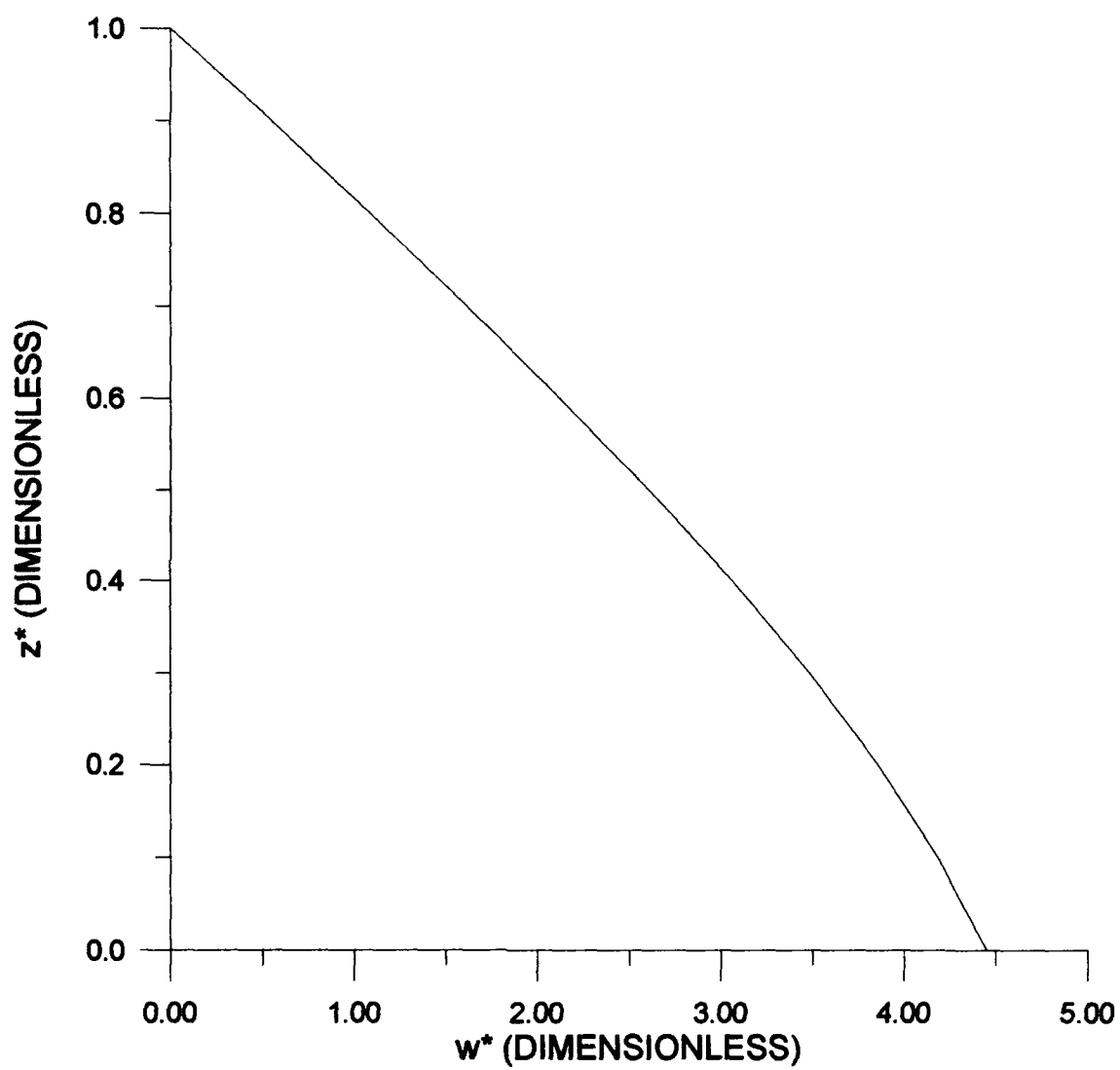


Fig. 3.14. Vertical velocity profile for the center of an updraft.

## Chapter 4

### CONCLUSIONS

The case study results in this thesis show that the model does in fact properly capture the spatial organization of the roll circulations and does correctly reproduce the vertical profiles of heat and momentum flux. We also showed that the temperature perturbation is a maximum at the lower boundary, just as we would expect when the primary heating source is located at the lower boundary. This result is in good agreement with the findings of Schmidt and Schumann (1989) that are based on a study of a higher resolution LES model. Their Fig. 18 illustrates a temperature profile that does indeed have a temperature maximum at the lower boundary. Our results also reveal that the temporal periodicity of the system is consistent with both physical and numerical analyses of the solution based on advection by the cross-roll mean wind. These results indicate that the system of equations used and many of the physical assumptions made are appropriate for modeling boundary layer rolls in a marine environment.

Although the model did capture many of the expected aspects of the circulation, there are two distinct results that point to the need for further analysis and model redesign. One of the significant results of the model integrations is that we could not find a bifurcating solution that came into a state of equilibration. As mentioned earlier, there seems to be a source of energy that is not being damped properly by the model. Early investigation points to excessive growth of the nonlinear term in some of the thermodynamic equations. This growth manifests itself as a rapid increase in the magnitude of the temperature amplitude coefficient  $T_{01}$  that represents the modification of the linear temperature profile by the roll circulations. Although in the case of the damping solution used for our case study  $T_{01}$  did equilibrate, it was to a value that greatly exceeded

the magnitudes of the other temperature amplitude coefficients. This mysterious source of energy may be a result of a computer coding error, although we performed many integrations using symmetry tests to identify and eliminate this type of error. There is also a chance that a numerical instability causes the solution to grow infinitely. We did add a numerical dissipation term, as described in Chapter 2, that seemed to control the growth and so allowed us to at least find a damping solution.

The other major concern suggested by the model integrations is the inconsistency in the velocity field at the lower boundary. The vertical velocity profile indicates that a maximum in upward or downward motion occurs at the lower boundary. This maximum however should occur somewhere near the midpoint of the vertical domain, as confirmed for example by Fig. 18 of Schmidt and Schubert (1989) and Figs. 2.1-2.2.

There are two ways of accepting as physically plausible the results of the present model, although neither conform to the original concept. First, if we were to consider the lower boundary to be near the midpoint of the boundary layer, then the maximum vertical velocity occurring below it would be consistent with observations. Second, if we limited our domain height severely to be within the lowest part of the boundary layer and were interested in the growth of the circulation, then at some point the vertical velocity maximum would occur below 10 *m* as given by our model results.

To meet our original intent, however, we must re-evaluate our application of the new boundary conditions, which not only use nonzero boundary values at the lower boundary, but rely on surface layer similarity theory to specify the constants in them. For example, there may be a problem in how the values of the lower boundary forcing constants,  $s_m$  and  $s_T$ , are determined. An energetics analysis may point to a problem in how these constants contribute to the boundary source and sink terms that result from integration by parts. The more likely problem is, however, that the way in which we apply

the similarity theory does not result in a proper representation of vertical fluxes at the lower boundary.

Upon further reflection, it seems likely that the similarity theory, which is used to describe the dynamics within the lowest 100 *m* of the boundary layer, may not properly represent the velocity scaling we need for specifying the lower boundary conditions for kilometer-scale circulations. The solutions we are modeling fill the entire boundary layer and so scale with boundary layer depth. It thus seems more appropriate to use convective scaling to specify the lower boundary conditions for velocity.

Mathematically, similarity theory gives us positive values for the two constant forcing parameters when the boundary layer is unstable. This forces the vertical profiles for temperature and vertical velocity to take the form of the vertical basis functions given in Figs. 3.1-3.2. As we stated earlier, the vertical profile for temperature is consistent with what we expect at the lower boundary. A maximum of temperature at the lower boundary follows from the fact that  $T^*$  and  $\partial T^* / \partial z^*$  at  $z^* = 0$  have opposite signs when  $s_T > 0$ . This fact can be seen by assuming  $T \sim \cos(z/z_T)$  at  $z = 10$  *m*, which is a form having largest values at  $z^* = 0$ . The vertical profile for vertical velocity, however, does not allow us to obtain a maximum above the height of the lower boundary because  $w^*$  and  $\partial w^* / \partial z^*$  have opposite signs when  $s_w > 0$ . The only way to move the maximum in  $w^*$  into the domain is to reverse the sign of the velocity constant forcing parameter  $s_w$  in (2.35)-(2.37), which is easily seen by assuming  $w \sim \sin(z/z_T)$  at  $z = 10$  *m* as suggested by Figs. 2.1-2.2.

Hopefully, we can solve the above boundary condition problem by employing convective scaling theory to specify the lower boundary conditions for velocity (e.g. Stull 1988). We hypothesize that this scaling theory would give a velocity constant forcing parameter  $s_w$  that is negative and would produce vertical basis functions that yield a maximum in vertical velocity above the lower boundary. Although our model did provide

an accurate representation of the heat and momentum flux profiles, we must recognize that the structure of these profiles may be correct even with qualitatively incorrect representations of vertical velocity. Until the boundary conditions are correctly specified to produce an accurate vertical velocity profile, we cannot study the stress variability pattern at the sea surface.

## REFERENCES

- Brown, R. A., 1980: Longitudinal instabilities and secondary flows in the planetary boundary layer: A review. *Rev. Geophys. Space Phys.*, **18**, 683-697.
- Brümmer, B. and B. Busack, 1990: Convective patterns within a field of stratocumulus. *Mon. Wea. Rev.*, **118**, 801-817.
- Gerling, T. W., 1985: Remote sensing of the ocean-surface wind field with a scatterometer and a synthetic aperture radar. *John Hopkins APL Digest*, **6**, 320-329.
- Gerling, T. W., 1986: Structure of the surface wind field from the Seasat SAR. *J. Geophys. Res.*, **91**, 2308-2320.
- Haack, T. and H. N. Shirer, 1992: Mixed convective-dynamic roll vortices and their effects on initial wind and temperature profiles. *J. Atmos. Sci.*, **49**, 1181-1201.
- Higgins, R. W., 1987: From the equations of motion to spectral models. *Nonlinear Hydrodynamic Modeling: A Mathematical Introduction. Lecture Notes in Physics*, **271**, H. N. Shirer, Ed., Springer-Verlag, 47-69.
- Laufersweiler, M. J. and H. N. Shirer, 1989: A simple dynamical model of a stratocumulus-topped boundary layer. *J. Atmos. Sci.*, **46**, 1133-1153.
- Lilly, D. K., 1966: On the instability of Ekman boundary flow. *J. Atmos. Sci.*, **23**, 481-494.
- Pyle, R. J., 1987: Typical branching forms: Periodic solutions. *Nonlinear Hydrodynamic Modeling: A Mathematical Introduction. Lecture Notes in Physics*, **271**, H. N. Shirer, Ed., Springer-Verlag, 264-291.
- Schmidt, H. and U. Schumann, 1989: Coherent structure of the convective boundary layer derived from large-eddy simulations. *J. Fluid Mech.*, **200**, 511-562.
- Shirer, H. N., 1986: On cloud street development in three dimensions: Parallel and Rayleigh instabilities. *Contrib. Atmos. Phys.*, **59**, 126-149.
- Shirer, H. N., Ed., 1987: *Nonlinear Hydrodynamic Modeling: A Mathematical Introduction. Lecture Notes in Physics*, **271**, Springer-Verlag, 546 pp.

- Stensrud, D. J., 1987: The expected branching solution: Preferred wavelengths and orientations. *Nonlinear Hydrodynamic Modeling: A Mathematical Introduction. Lecture Notes in Physics*, 271, H. N. Shiner, Ed., Springer-Verlag, 292-324.
- Stensrud, D. J. and H. N. Shiner, 1988: Development of boundary layer rolls from dynamic instabilities. *J. Atmos. Sci.*, 45, 1007-1019.
- Stull, R. B., 1988: *An Introduction to Boundary Layer Meteorology*. Kluwer Academic Publishers, Boston, 666 pp.
- Visecky, J. F. and R. H. Stewart, 1982: The observation of ocean surface phenomena using imagery from the SEASAT synthetic aperture radar: An assessment. *J. Geophys. Res.*, 87, 3397-3430.

## Appendix A

### DETERMINING THE CONSTANTS IN THE BOUNDARY CONDITIONS

The boundary conditions used in the nonlinear dynamic model are based on the surface layer similarity theory from Stull (1988). Two empirical convective surface layer relationships are used,

$$\frac{kz}{u_*} \frac{\partial u}{\partial z} = \left(1 - 16 \frac{z}{L}\right)^{-1/4} = \mathcal{G}_m \left(\frac{z}{L}\right) \quad (\text{A.1})$$

$$\frac{kz}{T_*} \frac{\partial T}{\partial z} = 0.74 \left(1 - 9 \frac{z}{L}\right)^{-1/2} = \mathcal{G}_n \left(\frac{z}{L}\right), \quad (\text{A.2})$$

where  $k$  is the von Karman constant,  $z$  is the height above the surface,  $u$  is the mean roll-scale wind speed,  $u_*$  is the friction velocity,  $L$  is the Monin-Obukhov length,  $T$  is the mean roll-scale temperature, and  $T_*$  is the surface layer temperature scale.

The boundary conditions were developed by Ms. Julie L. Schramm. Her goal was to make the boundary conditions (2.34)-(2.39) consistent with the similarity relationships given in (A.1)-(A.2). The relationship in (A.1) is solved for  $u$  giving the equation

$$u(z) = \frac{u_*}{k} \left[ \ln \frac{z}{z_0} - \Psi_m \left( \frac{z}{L} \right) \right], \quad (\text{A.3})$$

where

$$\Psi_m\left(\frac{z}{L}\right) = \int_{z/L}^{z_0/L} \left[1 - \mathcal{G}_m\left(\frac{z}{L}\right)\right] \frac{d(z/L)}{z/L}. \quad (\text{A.4})$$

We then use (A.4) and its derivative to eliminate  $u_*/k$  to give

$$u(z) = \frac{\partial u}{\partial z} \frac{[\ln(z/z_0) - \Psi_m(z/L)]}{\{1/z - \partial[\Psi_m(z/L)]/\partial z\}}. \quad (\text{A.5})$$

Here  $\Psi_m(z/L)$  and  $\partial[\Psi_m(z/L)]/\partial z$  are obtained from (A.4) using the definition (A.1) of  $\mathcal{G}_m(z/L)$ , and the integral evaluation routine from the DERIVE software package. The equation (A.5) can thus be expressed in the form

$$u(z) = \frac{\partial u}{\partial z} f_m(z, z_0, L). \quad (\text{A.6})$$

We next introduce the relationships

$$u = \frac{u^* \kappa}{z_T - h_{LB}} \quad (\text{A.7})$$

$$z = z^*(z_T - h_{LB}) + h_{LB}, \quad (\text{A.8})$$

where  $z_T$  is the height of the top of the boundary layer and  $h_{LB}$  is the height of the lower boundary. Equation (A.6) now takes the form

$$u^*(z^*) = \frac{\partial u^*}{\partial z^*} f_m(z^*, z_T, z_o, h_{LB}, L). \quad (\text{A.9})$$

The function  $f_m(z^*, z_T, z_o, h_{LB}, L)$  is evaluated at  $z^* = 0$ , which corresponds to the height  $z = h_{LB}$ . The parameter values  $z_o$  and  $L$  are determined from a subroutine supplied by Dr. George S. Young. This subroutine was implemented by Mr. Dave V. Ledvina during his thesis research based on work done by Dr. Chris W. Fairall. The subroutine uses input values for the mean wind speed, humidity difference, and temperature difference at the lower boundary to calculate  $z_o$  and  $L$ . The evaluated function  $f_m(0, z_T, z_o, h_{LB}, L)$  will be referred to as the Schramm momentum constant,  $s_m$ , which now represents the forcing of the wind by surface layer eddies at the lower boundary. Example subroutine input values, calculated values for  $z_o$  and  $L$ , and associated Schramm momentum constants are given in Chapter 3.

The new velocity boundary conditions for the lower boundary that apply to both the  $u$  and  $v$  components of the wind are then

$$u^*(0) - s_m \frac{\partial u^*(0)}{\partial z^*} = 0 \quad (\text{A.10})$$

$$v^*(0) - s_m \frac{\partial v^*(0)}{\partial z^*} = 0, \quad (\text{A.11})$$

but the one for the  $w$  component is given through use of the continuity equation by

$$\frac{\partial w^*(0)}{\partial z^*} - s_m \frac{\partial^2 w^*(0)}{\partial z^{*2}} = 0. \quad (\text{A.12})$$

Upper boundary conditions must be applied at  $z^* = 1$ , which corresponds to the height  $z = z_T$ . We assume a rigid stress-free boundary so that

$$\frac{\partial u^*(1)}{\partial z^*} = \frac{\partial v^*(1)}{\partial z^*} = w^*(1) = 0. \quad (\text{A.13})$$

Boundary conditions for temperature are found with a similar method. The temperature profile given in (A.2) may be solved for  $T$  giving the relationship

$$T(z) = \frac{T_*}{k} \left[ \ln \frac{z}{z_0} - \Psi_n \left( \frac{z}{L} \right) \right], \quad (\text{A.14})$$

where

$$\Psi_n \left( \frac{z}{L} \right) = \int_{z/L}^{z/L} \left[ 1 - g_n \left( \frac{z}{L} \right) \right] \frac{d(z/L)}{z/L}. \quad (\text{A.15})$$

We then use (A.15) and its derivative to eliminate  $T/k$  to give

$$T(z) = \frac{\partial T}{\partial z} \frac{[\ln(z/z_0) - \Psi_n(z/L)]}{\{1/z - \partial[\Psi_n(z/L)]/\partial z\}}. \quad (\text{A.16})$$

As with velocity, the equation can now be expressed in the form

$$T(z) = \frac{\partial T}{\partial z} f_T(z, z_0, L). \quad (\text{A.17})$$

This equation is now made dimensionless using the relationships

$$T = \frac{T^* \nu \kappa T_\infty}{g(z_T - h_{LB})^3} \quad (\text{A.18})$$

and (A.8), where  $\nu$  is the eddy viscosity,  $\kappa$  is the eddy thermometric conductivity, and  $T_\infty$  is the sea surface temperature. Equation (A.17) now takes the form

$$T^*(z^*) = \frac{\partial T^*}{\partial z^*} f_T(z^*, z_T, z_0, h_{LB}, L). \quad (\text{A.19})$$

The function  $f_T(z^*, z_T, z_0, h_{LB}, L)$  is evaluated at  $z^* = 0$  and is defined as the Schramm temperature constant,  $s_T$ , which represents the forcing of temperature at the lower

boundary. The new boundary condition for the lower boundary is then

$$T^*(0) + s_T \frac{\partial T^*(0)}{\partial z^*} = 0. \quad (\text{A.20})$$

We assume a perfectly conducting upper boundary so that

$$T^*(1) = 0. \quad (\text{A.21})$$

These boundary conditions are applied to the Stokes and Helmholtz problems to determine the vertical basis functions and their corresponding eigenvalues, as summarized in Appendix B.

## Appendix B

### VERTICAL BASIS FUNCTIONS AND EIGENVALUES

The vertical basis function and corresponding eigenvalues for temperature are determined by solving the Helmholtz problem

$$\gamma T^* = -\tilde{\nabla}^2 T^* \quad (\text{B.1})$$

with boundary conditions (A.20)-(A.21), where

$$\tilde{\nabla} = a_x \frac{\partial}{\partial x^*} \mathbf{i} + a_y \frac{\partial}{\partial y^*} \mathbf{j} + \frac{\partial}{\partial z^*} \mathbf{k}, \quad (\text{B.2})$$

$T^*$  is a dimensionless temperature eigenfunction, and  $\gamma$  is the corresponding eigenvalue.

We use separation of variables to find solutions of the form

$$T^* = \text{trig}_i(x^*, y^*) F_j(z^*), \quad (\text{B.3})$$

where

$$\text{trig}_0(x^*, y^*) = 1 \quad (\text{B.4})$$

$$\text{trig}_1(x^*, y^*) = \sin 2\pi x^* \sin 2\pi y^* \quad (\text{B.5})$$

$$\text{trig}_2(x^*, y^*) = \sin 2\pi x^* \cos 2\pi y^* \quad (\text{B.6})$$

$$\text{trig}_3(x^*, y^*) = \cos 2\pi x^* \sin 2\pi y^* \quad (\text{B.7})$$

$$\text{trig}_4(x^*, y^*) = \cos 2\pi l x^* \cos 2\pi m y^*, \quad (\text{B.8})$$

with horizontal wavenumbers  $l$  and  $m$ , and  $F_j(z^*)$  is a solution of the eigenvalue problem

$$\frac{\partial^2 F_j}{\partial z^{*2}} + (\gamma - \sigma^2) F_j(z^*) = 0 \quad (\text{B.9})$$

$$F_j(0) + s_T \frac{\partial F_j(0)}{\partial z^*} = 0 \quad (\text{B.10})$$

$$F_j(1) = 0, \quad (\text{B.11})$$

where

$$\sigma^2 = 4\pi^2 a_x^2 l^2 + 4\pi^2 a_y^2 m^2 \quad (\text{B.12})$$

$$\gamma - \sigma^2 = \lambda_j \quad (\text{B.13})$$

and  $\lambda_j$  is the eigenvalue of the vertical basis function  $F_j(z^*)$ . We number these eigenvalues by increasing value, starting with  $\lambda_1$  as the smallest.

When  $\lambda_j > 0$ , the solution is of the form

$$F_j(z^*) = A \sin \omega_j z^* + B \cos \omega_j z^*, \quad (\text{B.14})$$

where  $\omega_j^2 = \lambda_j$ , and  $A$  and  $B$  are constant coefficients. Applying the first boundary

condition (B.10) produces

$$B + s_T \omega_j A = 0. \quad (\text{B.15})$$

Applying the second boundary condition (B.11) gives

$$A \sin \omega_j + B \cos \omega_j = 0. \quad (\text{B.16})$$

Solving this system of equations yields

$$F_j(z^*) = \cos \omega_j z^* - \frac{1}{s_T \omega_j} \sin \omega_j(z^*), \quad (\text{B.17})$$

where

$$s_T \omega_j = \tan \omega_j. \quad (\text{B.18})$$

When  $s_T > 1$ , (B.14) represents the only solutions that exist. When  $s_T < 1$ , however, the first eigenvalue  $\lambda_1$  is negative. This eigenvalue and its associated vertical basis function  $F_1(z^*)$  are found by solving the differential equation

$$\frac{\partial^2 F_1}{\partial z^{*2}} - |\lambda_1| F_1(z^*) = 0, \quad (\text{B.19})$$

which has a solution of the form

$$F_1(z^*) = Ae^{\omega_1 z^*} + Be^{-\omega_1 z^*}, \quad (\text{B.20})$$

where  $\omega_1^2 = \lambda_1$  and  $A$  and  $B$  are constant coefficients. Applying the boundary conditions and solving the resulting pair of equations gives

$$F_1(z^*) = \cosh \omega_1 z^* - \frac{1}{s_T \omega_1} \sinh \omega_1 z^*, \quad (\text{B.21})$$

where

$$s_T \omega_1 = \tanh \omega_1. \quad (\text{B.22})$$

The vertical basis functions and corresponding eigenvalues for velocity are determined by solving the Stokes problem

$$\alpha P \alpha_x \mathbf{v}^* = -P \tilde{\nabla}^2 \mathbf{v}^* + \alpha_x \tilde{\nabla} p^* \quad (\text{B.23})$$

$$\tilde{\nabla} \bullet \mathbf{v}^* = 0. \quad (\text{B.24})$$

with boundary conditions (A.10)-(A.12), where  $P$  is the Prandtl number,  $p^*$  is the dimensionless pressure,  $\alpha_x$  is the aspect ratio in the  $x$  direction,  $\mathbf{v}^*$  is a dimensionless velocity vector eigenfunction, and  $\alpha$  is the corresponding eigenvalue. Equation (B.24) together with the boundary conditions imply that the velocity vector  $\mathbf{v}^*$  may be expressed

in terms of the curl of a vector streamfunction  $\mathbf{A}^*$ ; this vector streamfunction is defined as the sum of two vector streamfunctions,  $\boldsymbol{\psi}^*$  and  $\boldsymbol{\eta}^*$ , where

$$\boldsymbol{\psi}^*(x^*, y^*, z^*, t^*) = \sum_{p=0}^4 \sum_{q=1}^4 \psi_{pq}(t^*) \text{trig}_p(x^*, y^*) h_q(z^*) \mathbf{i} + 0\mathbf{j} + 0\mathbf{k} \quad (\text{B.26})$$

$$\boldsymbol{\eta}^*(x^*, y^*, z^*, t^*) = 0\mathbf{i} + \sum_{p=0}^4 \sum_{q=1}^4 \eta_{pq}(t^*) \text{trig}_p(x^*, y^*) h_q(z^*) \mathbf{j} + 0\mathbf{k} \quad (\text{B.27})$$

in the dimensionless coordinate system. The coefficients  $\psi_{pq}(t^*)$  and  $\eta_{pq}(t^*)$  are the temporally dependent amplitudes for the  $p$ th horizontally dependent trigonometric function and the  $q$ th vertical basis function. The definitions for the horizontally dependent trigonometric functions are given by (B.4)-(B.8). The function  $h_q(z^*)$  is the  $q$ th vertical basis function for which we are solving.

Next, we curl both sides of the Stokes equation to eliminate the pressure:

$$\alpha \tilde{\nabla} \times \mathbf{v}^* = -\frac{1}{\alpha_x} \tilde{\nabla}^2 (\nabla \times \mathbf{v}^*), \quad (\text{B.28})$$

We now substitute the definition for  $\mathbf{v}^*$ , which yields

$$\tilde{\nabla}^2 [\tilde{\nabla} \times (\tilde{\nabla} \times \mathbf{A}^*)] + \alpha_x \alpha \tilde{\nabla} \times (\tilde{\nabla} \times \mathbf{A}^*) = 0. \quad (\text{B.29})$$

We substitute for  $\mathbf{A}^*$  using equations (B.26)-(B.27), after applying separation of

variables, and expand the result to give the relationship

$$\frac{\partial^2 h_q}{\partial z^{*2}} + (a_x \alpha - \sigma^2) h_q(z^*) = 0, \quad (\text{B.30})$$

where

$$\sigma^2 = 4\pi^2 \alpha_x^2 l^2 + 4\pi^2 \alpha_y^2 m^2 \quad (\text{B.31})$$

$$a_x \alpha - \sigma^2 = \delta_q \quad (\text{B.32})$$

and  $\delta_q$  is the eigenvalue of the vertical basis function  $h_q(z^*)$ .

The vertical basis function and associated eigenvalues are now determined by solving the differential equation

$$\frac{\partial^2 h_q}{\partial z^{*2}} + \varpi_q^2 h_q(z^*) = 0, \quad (\text{B.33})$$

where  $\varpi_q^2 = \delta_q > 0$ , and by using the boundary conditions

$$\frac{\partial h_q(0)}{\partial z^*} - s_m \frac{\partial^2 h_q(0)}{\partial z^{*2}} = 0 \quad (\text{B.34})$$

$$h_q(1) = 0 \quad (\text{B.35})$$

derived in Appendix A. In this case we have arbitrarily chosen the boundary conditions for the velocity component  $w$ , although we could have chosen either of the other two velocity component boundary conditions. The solution to (B.33) is of the form

$$h_q(z^*) = C \sin \varpi_q z^* + D \cos \varpi_q z^*, \quad (\text{B.36})$$

where  $C$  and  $D$  are constant coefficients. Applying boundary condition (B.34) yields

$$\varpi_q C + s_m \varpi_q^2 D = 0, \quad (\text{B.37})$$

and applying boundary condition (B.35) gives

$$C \sin \varpi_q + D \cos \varpi_q = 0. \quad (\text{B.38})$$

Solving the pair of equations (B.37)-(B.38) results in the vertical basis function

$$h_q(z^*) = \cos \varpi_q z^* - s_m \varpi_q \sin \varpi_q z^*, \quad (\text{B.39})$$

where

$$s_m \varpi_q = \cot \varpi_q. \quad (\text{B.40})$$

In contrast to the temperature case, these are the only solutions that exist, regardless of the value of  $s_m$ . Thus the solutions always take the form (B.36).